VYSOKÉ UČENÍ TECHNICKÉ V BRNĚ

BRNO UNIVERSITY OF TECHNOLOGY

FAKULTA STROJNÍHO INŽENÝRSTVÍ
ÚSTAV MATERIÁLOVÝCH VĚD A INŽENÝRSTVÍ

FACULTY OF MECHANICAL ENGINEERING
INSTITUTE OF MATERIALS SCIENCE AND ENGINEERING

# MODIFICATION OF COATING-SUBSTRATE INTERFACE CHARACTER OF THERMALLY SPRAYED COATINGS USING ELECTRON BEAM TECHNOLOGY

MODIFIKACE CHARAKTERU ROZHRANÍ SUBSTRÁT-NÁSTŘIK VRSTEV DEPONOVANÝCH TECHNOLOGIEMI ŽÁROVÉHO NANÁŠENÍ POMOCÍ TECHNOLOGIE ELEKTRONOVÉHO PAPRSKU

DIPLOMOVÁ PRÁCE
MASTER'S THESIS

AUTOR PRÁCE — Bc. JIŘÍ MAREŠ
AUTHOR

VEDOUCÍ PRÁCE — Ing. JAN ČÍŽEK, Ph.D.
SUPERVISOR

BRNO 2015

Vysoké učení technické v Brně, Fakulta strojního inženýrství

Ústav materiálových věd a inženýrství
Akademický rok: 2014/2015

# ZADÁNÍ DIPLOMOVÉ PRÁCE

student(ka): Bc. Jiří Mareš

který/která studuje v **magisterském navazujícím studijním programu**

obor: **Materiálové inženýrství (3911T011)**

Ředitel ústavu Vám v souladu se zákonem č.111/1998 o vysokých školách a se Studijním a zkušebním řádem VUT v Brně určuje následující téma diplomové práce:

**Modifikace charakteru rozhraní substrát-nástřik vrstev deponovaných technologiemi žárového nanášení pomocí technologie elektronového paprsku**

v anglickém jazyce:

**Modification of coating-substrate interface character of thermally sprayed coatings using electron beam technology**

Stručná charakteristika problematiky úkolu:

Technologie žárového nanášení vrstev jsou osvědčenou skupinou procesů, při kterých je na daný materiál nanesena ochranná či funkční vrstva pokročilých materiálů v tloušťkách od 100 um do 5 mm.

Klíčovým faktorem pro aplikační uplatnění těchto komponent je charakter přilnutí vrstvy k substrátu. S pomocí využití technologických možností na ústavu dostupné technologie elektronového paprsku bude úkolem této práce pokusit se modifikovat charakter rozhraní substrát-nástřik a zhodnotit změnu v tomto charakteru (např. i zhodnocení změny adhezivní síly dle standardizované metody).

Cíle diplomové práce:

- seznámit studenta s technologiemi žárového nanášení, jejich příslušnými přednostmi a nevýhodami
- seznámit se s problematikou adheze depozitů, faktory ovlivňujícími její kvalitu a procesy k její modifikaci
- na připravených vzorcích se pokusit přetavením či jinými způsoby modifikovat rozhraní substrát-nástřik technologií elektronového paprsku pro zkvalitnění adhezní přilnavosti vrstev
- pokusit se vyhodnotit dopad provedených úprav na kvantitativní ukazatele adhezní síly

Seznam odborné literatury:

1. Tucker: ASM Handbook 5A: Thermal Spray Technology, ASM International, 2013
2. Papyrin, Kosarev, Klinkov, Alkhimov, Fomin: Cold Spray Technology, Elsevier, 2007
3. ASTM C-633-01 (2008): Adhesion or Cohesion Strength of Thermal Spray Coatings, ASTM International
4. Dickinson, Yamada: A New Method for Measuring Shear Adhesion Strength of Ceramic Cold Spray Splats, Nanosci Nanotechnol Lett, 2010, 2(4), p.348-351

Vedoucí diplomové práce: Ing. Jan Čížek, Ph.D.

Termín odevzdání diplomové práce je stanoven časovým plánem akademického roku 2014/2015.

V Brně, dne 19.11.2014

L.S.

| | |
|---|---|
| prof. Ing. Ivo Dlouhý, CSc.<br>Ředitel ústavu | doc. Ing. Jaroslav Katolický, Ph.D.<br>Děkan fakulty |

ABSTRACT

This thesis is focused on a modification of the coating-substrate interface of NiCrAlY bond-coats deposited by water stabilized plasma technology on S235JRC+C steel substrates. Electron beam remelting was chosen as the technology used for the modification and two different modifications were investigated. Attempt has been made to determine the effect of remelting on the adhesive strength of the coatings. Further analysis of the microstructure, phase and chemical composition and microhardness were carried out in the state prior and after the modification.

During the study it was found that change in phase composition occurs after the deposition as well as after the electron beam modification. It was also found that the electron beam modification caused melting of oxides in the coating original microstructure and resulted in resolidification of these oxides on the surface of the modified layer. Further it was found that electron beam modification resulted in decreased microhardness of the coatings due to oxide removal from the microstructure and coating-substrate material mixing.

Adhesive strength of the coatings in as-sprayed condition was quantified, however in the case of electron beam modified coatings the adhesive strength could not be fully quantified due to premature failure at the coating-adhesive agent interface during adhesion testing.

ABSTRAKT

Tato práce je zaměřena na modifikaci charakteru rozhraní substrát-nástřik NiCrAlY povlaků nanesených pomocí technologie vodou stabilizované plazmy na substráty z oceli S235JRC+C. Přetavení žárové vrstvy elektronovým paprskem bylo zvoleno jako technologie pro modifikaci a dvě různé modifikace byly zkoumány. V práci byl proveden pokus o stanovení vlivu modifikací na adhezní vlastnosti nástřiku. Dále jsou v práci prezentovány analýzy mikrostruktury, fázového a chemického složení a mikrotvrdosti ve stavu před a po modifikaci.

Během studie bylo zjištěno, že dochází ke změnám fázového složení jak během depozice, tak během modifikace elektronovým paprskem. Modifikace elektronovým paprskem způsobila roztavení oxidů původní mikrostruktury nástřiku, které následně rekrystalizovaly na povrchu modifikované vrstvy. Dalším získaným poznatkem bylo, že dochází ke snížení mikrotvrdosti po modifikaci, což bylo způsobeno odstraněním oxidů z mikrostruktury a promícháním materiálu substrátu a původního nástřiku.

Adheze nástřiků v as-sprayed stavu byla kvantifikována. V případě nástřiků modifikovaných elektronovým paprskem přesná kvantifikace nebyla možná, z důvodu předčasného porušení na rozhraní nástřik-adhezivní pojivo během adhezních testů.

KEY WORDS

Thermal spray, water-stabilized plasma spray, WSP, adhesion testing, electron beam, interface, NiCrAlY, coatings

KLÍČOVÁ SLOVA

Žárové technologie, vodou stabilizovaná plazma, WSP, adhezní zkoušení, elektronový svazek, rozhraní, NiCrAlY, povlak

## Bibliografická citace

MAREŠ, J. *Modifikace charakteru rozhraní substrát-nástřik vrstev deponovaných technologiemi žárového nanášení pomocí technologie elektronového paprsku.* Brno: Vysoké učení technické v Brně, Fakulta strojního inženýrství, 2015. 61 s. Vedoucí diplomové práce Ing. Jan Čížek, Ph.D..

## Čestné Prohlášení

Prohlašuji, že jsem diplomovou práci vypracoval samostatně na základě uvedených literárních pramenů a konzultací s vedoucím diplomové práce.

V Brně dne ……

Mareš Jiří

## Poděkování

Tímto bych chtěl poděkovat panu Ing. Janu Čížkovi, Ph.D za jeho pomoc a rady poskytnuté pro vypracování této diplomové práce. Dále bych chtěl poděkovat panu Ing. Josefu Zapletalovi, Ph.D za jeho pomoc při návrhu přípravku na lepení a za pomoc při adhezních testech. Také bych chtěl také poděkovat panu Ing. Radku Mušálkovi Ph.D a jeho týmu za depozici nástřiků a také panu Bc. Janu Kouřilovi za pomo v při přetavování nástřiků elektronovým paprskem. Poděkovat bych chtěl také panu Mgr. Janu Čuperovi, panu Ing. Janu Věžníkovi, slečně Ing. Petře Hanusové a panu Ing. Zdeňku Spotzovi, Ph.D za pomoc při analýzách použitých v experimentální části.

Na závěr bych chtěl poděkovat také své rodině, za podporu během celého mého studia.

# Table of Contents

# 1. Introduction

Materials have always been pushed to their limits and their properties are often limiting when it comes to using technologies. Limiting not only in the sense of its mechanical or chemical properties, but also economically. When we consider for example corrosion resistance it is the surface that is subjected to the surrounding harsh environment while the bulk of the material stays intact.

For this reason coating technologies have been developed. These are generally economically efficient way to get a workpiece with desired surface properties while the part itself can be made out of a much cheaper material than it would have to be in not coated condition. Further development of coating technologies led to applications that achieve combination of surface/bulk material properties that otherwise would not be possible. For this concept to work however, the coating adhesion to the workpiece is crucial. That is why this work is focused on modification of coating/substrate interface of plasma sprayed coatings and investigates influence of electron beam coating/interface modification on overall adhesion of the coating to the substrate.

In the literature review section plasma sprayed technology and coating formation are discussed. Later its adhesion mechanisms are discussed along with thermal barrier coating systems with MCrAlY bond coats and electron beam technology. Further in the experimental part of this work, effect of electron beam modification of plasma sprayed MCrAlY bond coats on its characteristics will be studied. Particularly microhardness, coating microstructure using light and electron microscopy, adhesion, and chemical composition using EDX and XDR analysis.

# 2. Literature Research

## 2.1. Thermal Spray Technology

This wide group of technologies is used to apply metallic or nonmetallic coatings. Each technology differs by the energy source used to heat the coating material (depending on the technology, the coating material is supplied in powder, wire or rod form). Therefore temperatures of the processes differ widely as well as the deposition velocities. The power of thermal spray technologies is in its high flexibility, which makes it possible to apply almost any material onto almost and substrate resulting in a wide range of applications. Those are for example [1]:

- Wear resistant coatings
- Thermal insulation
- Corrosion resistance
- Abradables and abrasives
- Electrically conductive coatings
- Electrically resistive/insulating coatings
- Dimensional restoration coatings
- Bio-medical coatings

### 2.1.1. Brief History

The origins of thermal spray technology date back to patents registered in 1882 - 1889 by M. U. Schoop (Zurich, Switzerland) for a process that fed lead and tin wires into a modified oxyacetylene welding torch later modified further to accept powdered materials. Eventually, electric arc spray technology was patented in 1908 (also by Schoop) which allowed more metals to be sprayed [1].

However, significant expansion of thermal spray technology occurred not until after the World War II, when the plasma spray was developed. Reinecke was the first to demonstrate that powders injected into a plasma arc gas heater could create molten particles, which could be accelerated toward a surface to form a coating (first plasma spray coating in 1939) [1]. The advantages of plasma spray were high process temperatures compared to the combustion spray jet, independence of the material feed from the heat source and higher particle speeds [1]. Later technologies like detonation gun (D-gun) and HVOF were developed [1].

### 2.1.2. Thermal Spray Processes

Each thermal spray technology uses concentrated heat source to melt feedstock materials and propel molten particulates towards prepared substrate using jets. Process technologies are differentiated by these energy sources. The source may be combustion of fuels with oxygen or air, electrical arc or plasma. Standalone category is cold spray, where feedstock material is given enough kinetic energy to surpass so called critical velocity and adhere to the substrate surface even without in-flight melting. Different thermal spray processes are compared in Table 1 [1, 2].

**Table 1 – Overview of thermal spray technologies [1]**

| Attribute | Flame spray | High-velocity oxyfuel | Detonation gun | Wire arc | Air plasma | Vacuum plasma | Radiofrequency plasma |
|---|---|---|---|---|---|---|---|
| **Jet** | | | | | | | |
| Jet temperature, K | 3500 | 5500 | 5500 | >25,000 | 15,000 | 12,000 | 10,000 |
| Jet velocities, m/s (ft/s) | 50–100 (160–300) | 500–1200 (1600–4000) | >1000 (>3300) | 50–100 (160–300) | 300–1000 (1000–3300) | 200–600 (700–2000) | 20–80 (70–300) |
| Gas flow, sLm | 100–200 | 400–1100 | N/A | 500–3000 | 100–200 | 150–250 | 75–150 |
| Gas types | $O_2$, acetylene | $CH_4$, $C_2H_6$, $H_2$, $O_2$ | $O_2$, acetylene | Air, $N_2$, Ar | Ar, He, $H_2$, $N_2$ | Ar, He, $H_2$ | Ar, He, $H_2$ |
| Power input, kW equiv. | 20 | 150–300 | N/A | 2–5 | 40–200 | 40–120 | 40–200 (plate) |
| **Particle feed** | | | | | | | |
| Particle temperature (max), °C (°F) | 2500 (4500) | 3300 (6000) | N/A | >3800 (>6900) | >3800 (>6900) | >3800 (>6900) | >3800 (>6900) |
| Particle velocities, m/s (ft/s) | 50–100 (160–300) | 200–1000 (700–3300) | N/A | 50–100 (160–300) | 200–800 (700–2600) | 200–600 (700–2000) | 20–50 (70–160) |
| Material feed rate, g/min | 30–50 | 15–50 | N/A | 150–2000 | 50–150 | 25–150 | 20–50 |
| **Deposit/coating** | | | | | | | |
| Density range (%) | 85–90 | >95 | >95 | 80–95 | 90–95 | 90–99 | 95–99 |
| Bond strength, MPa (ksi:) | 7–18 (1–3) | 68 (10) | 82 (12) | 10–40 (1.5–6) | <68 (<10) | >68 (>10) | >68 (>10) |
| Oxides | High | Moderate to dispersed | Small | Moderate to high | Moderate to coarse | None | None |

## 2.1.3. Plasma Spray Technology

This type of technology uses plasma, a gas heated to high temperatures causing its molecules to ionize and, as a result, the gas becomes electrically conductive [3]. The plasma gas rapidly expands through a nozzle and a plasma jet is created. This technology is one of the most versatile among the thermal spray technologies as it enables to spray basically any material [1]. The specifics of the plasma spray process are dependent on the plasma torch design which varies widely. The main differences in the plasma torch design are [4]:

- Energy source (D.C. or Radio Frequency)
- Power input levels (20 - 200+ kW)
- Arc stabilization (gas, water, axial or vortex flow)
- Gas speed (supersonic or subsonic)
- Powder injection (internal axial or external radial)

### Plasma Forming Gasses

Generally mandatory condition to achieve sustainable plasma is such that, at atmospheric pressure, its electrical conductivity is higher than $10^3$ $S.m^{-1}$. The most commonly used plasma spray gasses and gas mixtures are Ar, Ar-He, $N_2$-$H_2$, Ar-$H_2$ [4]. For these gasses this condition is achieved as soon as the plasma gas temperature is higher than 8000 K [4]. Plasma temperature depends on its enthalpy and is calculated as power dissipated $P_g$ in the gas divided by plasma-gas mass flow rate $\dot{m}g$ (eq. 1):

$$T = \frac{P_g}{\dot{m}g} = \frac{V \cdot I - Q_e}{\dot{m}g} \qquad (1)$$

Where $V$ is the arc voltage, $I$ is the arc current and $Q_e$ are losses in the cooling unit, $\dot{m}g$ is the plasma-gas mass flow rate and $T$ is the temperature of the plasma gas. A

temperature of 8000 K corresponds to minimum critical enthalpy ($H_c$) and strongly depends on the plasma gas composition as can be seen in the Figure 1.

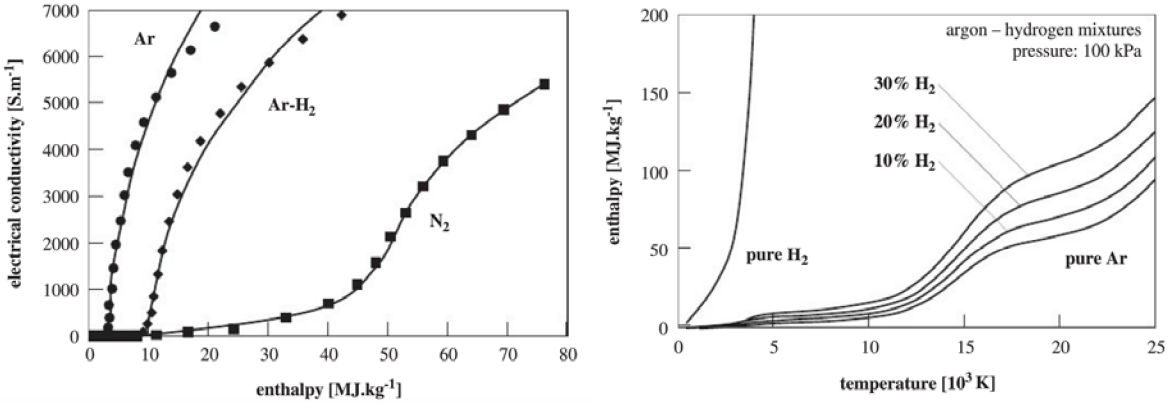


**Figure 1 - Left - Evolution of plasma electrical conductivity versus gas mass enthalpy. Right - Evolution of mass enthalpy of certain gasses and gas mixtures versus the plasma temperature [4]**

It is worth noting that monoatomic gasses generally have lower enthalpy than molecular gasses. That is because molecular gasses need energy to dissociate before they start to ionize. Gas composition has to be tailored to the material that is being injected into the gas flow, so the right amount of heat and momentum is transferred to the injected powder. As can be seen in Figure 1 argon has the lowest enthalpy of the mentioned gasses, but because of its low heat conductivity hydrogen in 10-30% vol. is added. Hydrogen however has low molecular mass and could impair plasma jet momentum which drives the acceleration of the injected feedstock material, therefore reasonable balance has to be found [1, 4].

## Arc root Stabilization

For torches that use D.C. as an energy source electric arc stability is a major concern. The arc plasma is easily influenced by asymmetric cooling or by effects of magnetic fields. The dominant effect is the drag force exerted by the cold gas in the boundary layer that develops at the cooled anode wall. Combination of these effects can cause an arc-anode attachment extinction. Generally there are three types of arc-anode attachment movements and those are (Figure 2) [4, 5]:

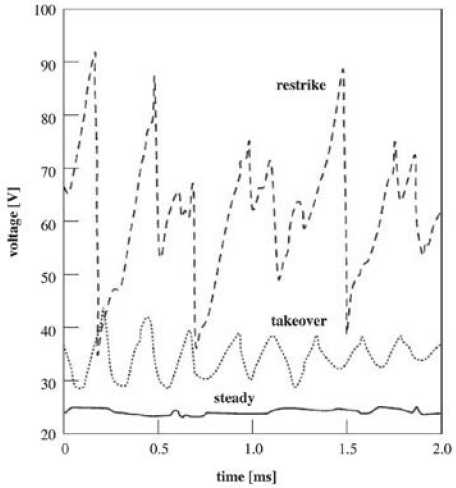


**Figure 2 - Voltage-time evolution of different modes linked to arc root fluctuations at the anode [4]**

- Steady mode (poor anode lifetime)
- Take over mode (mostly with monatomic plasma gas)
- Restrike mode (mostly occurring with diatomic plasma gas)
- The mixed mode (combination of all three or two of the modes)

Arc can be stabilized by a cylindrical wall (e.g. water cooled metal) or by flow stabilization when vortex flow is used. The vortex keeps the light high temperature gases at the flow axis while the heavier cold gases are flowing along the anode wall. These two methods are usually combined in plasma torches.

### Direct Current Stick Type Cathode torch

The direct current (DC) plasma arc gun combines radially aligned cathode frequently made of thoriated tungsten and an anode/nozzle oxygen-free high purity copper (OFHC) (Figure 3). Tungsten is a good thermionic emitter and has a high melting point of 3695 K [1]. The anode is typically made of OFHP copper sometimes combined with insert made of tungsten [4].

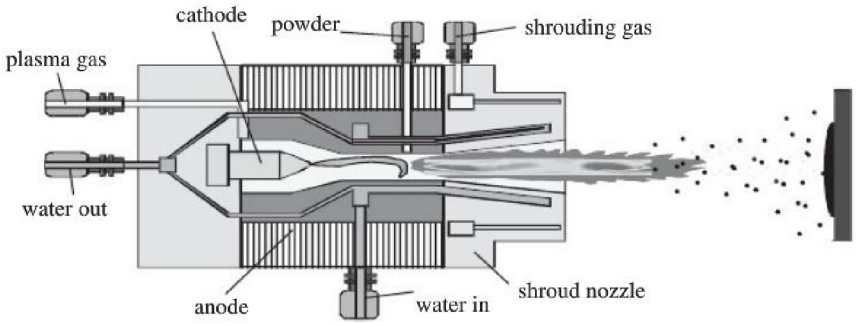


**Figure 3 - DC plasma torch design [4]**

### Radio Frequency (RF) Plasma Spray Torches

The radio-frequency plasma spray torches are taking advantage of the same phenomena that is being used in induction heating of metals. These torches have no electrodes and are built of a hollow glass or ceramic tube usually around 50 mm in diameter and 150 mm in length surrounded by an induction coil that is connected to a high frequency current generator [4, 6]. The gas and powder are injected at one end of the tube and the particles of the powder are induction heated while passing through the tube [4]. Due to large diameter of the nozzle compared to other designs, the injected powder velocities achieved are lower [6]. Schematically drawn RF torch can be seen in Figure 4.

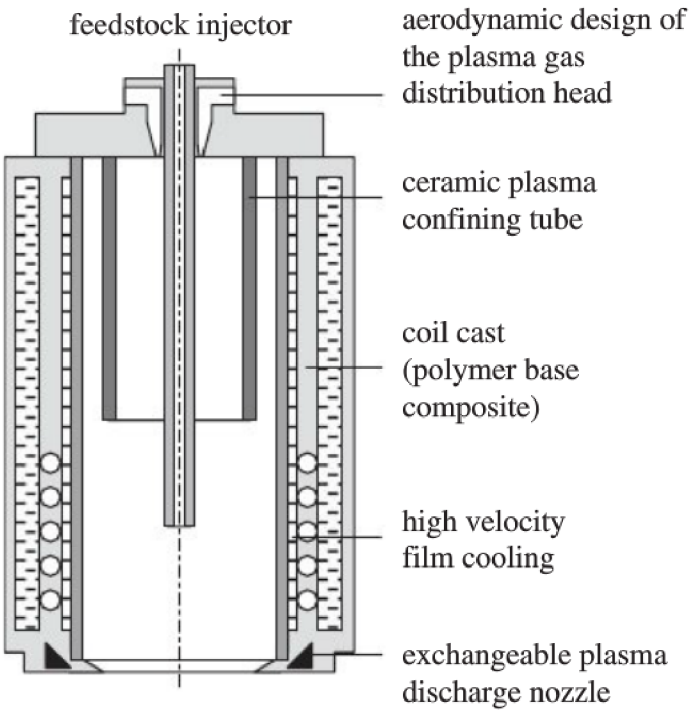


**Figure 4 - RF plasma torch design [4]**

### Water-Stabilized Plasma Torch

In regular plasma torch designs, the plasma gas temperature and enthalpy is limited as the flowing gas protects the arc chamber walls from thermal overloading and thus a minimum possible gas flow rate exists for given arc power. This is solved in WSP by water injection that stabilizes the arc instead of using gas. The walls of the chamber are then formed by water, which continuously evaporates. Water is dissociated by the arc and the result is ionized oxygen and hydrogen that forms the plasma. Because of the plasma composition this leads to a creation of high temperature and enthalpy plasma jet [7]. Significant development began in the Czech Republic in the mid-1980s by P. Chraska and continues up to this day [1, 4].

Schematic picture of the WSP torch can be seen in the Figure 5. The water is injected tangentially and a water vortex is created. The cathode is made out of a graphite rod and the anode is made of copper disc, which has internal cooling and rotates to reduce strong electrode erosion in the steam plasma. This torch is best suited for spraying large-scale oxide ceramic coatings. However, metals (such as NiCrAlY bond-coats) and cermets can also be sprayed by WSP [4, 7].

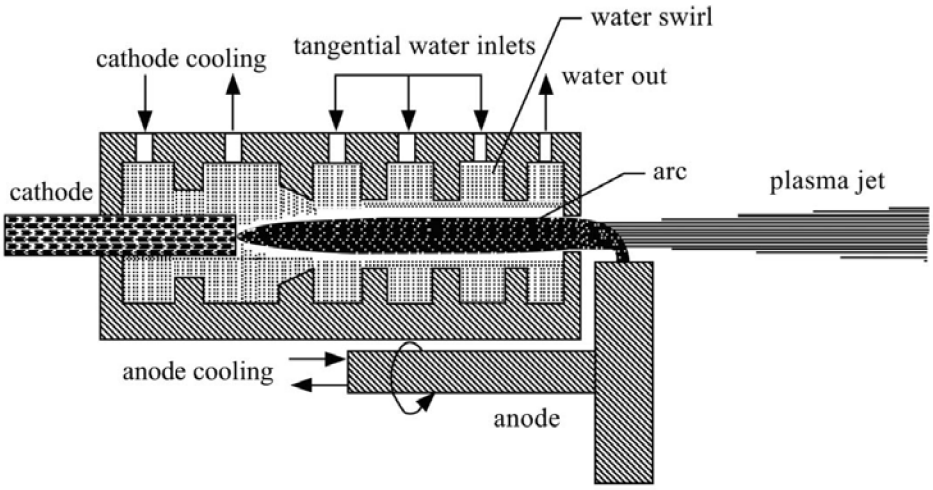


**Figure 5 - Water stabilized plasma torch design [7]**

## 2.1.4. Plasma Sprayed Coating Formation and Characteristics

Plasma spraying is a complex process and to fully understand the coating structure and its origin the process has to be understood as a whole. That is why the first part of this chapter is devoted to interactions of feedstock material with its surrounding atmosphere that occur during spraying. This is followed by discussion of what happens after the sprayed material impacts the surface and in the end of the chapter, final coating structure is discussed.

### In Flight Particle Interactions

Because the material is melted when heated by the plasma, different types of interactions take place between the particles and its surrounding atmosphere. Fluid mechanics becomes relevant and qualities like kinematic viscosity of the gas and melted material, Reynolds number *Re* (defined in eq. 2) and Webber number *We* (defined in eq. 3) become important [4].

$$Re = \frac{\rho V_0 D_0}{\mu} \quad (2)$$

$$We = \frac{\rho V_0^2 D_0}{\sigma} \quad (3)$$

Where $D_0$ is initial droplet diameter, $V_0$ is impact velocity, $\rho$ is liquid density, $\mu$ represents liquid viscosity and $\sigma$ stands for liquid-gas surface tension.

As the powder enters the plasma jet, it immediately starts to gain kinetic and thermal energy from the plasma. Particles enter the plasma hot core, their surface is rapidly heated, and reaches the melting point in approximately 0,1 ms [8]. This time is relatively small compared to the time needed for latent heat dissipation during melting. This is not a problem for materials with high thermal conductivity (e.g. metals that also have high diffusivity) but in case of ceramic materials, large differences in surface, core and melting front temperatures start to develop due to its low thermal conductivity and high melting point. This often results in not fully melted particles [8].

Another important aspect of melted particle interaction with its surrounding atmosphere is oxidation. There are two mechanisms governing this reaction. Generally it is controlled by diffusion, however if Reynolds number is higher than 20 and ratio of kinematic viscosities of the plasma and particle is higher than 50, a convective phenomenon is induced within the particle. That means the oxide forming on the particle surface is continuously being entrained into the particle so the surface is being continuously supplied with fresh metal [5, 9]. Oxides then form nodules inside the particle and the oxide phase is well distinguishable from the particle material due to high surface tension. Apart from oxidation, nitridation has also been proven to happen during plasma spraying in several cases [8, 10].

When using materials with relatively low vaporization temperature during plasma spraying some fraction of the material may evaporate, especially small particles as they require smaller thermal energy input and dwell times to get into the vapor phase. This phenomenon is called selective vaporization. This can sometimes cause problems as some elements in the feedstock material may evaporate faster than others resulting in chemical composition differences of the coating when compared to the composition of the feedstock material [3]. This phenomena also causes lower deposition efficiency. Material that is vaporized can either be oxidized into an oxide or it condenses back into ultra-fine (sub-micron) particles. In the Figure 6 on the right it can be seen that number of submicronic particles increases significantly with greater distance from the plasma torch nozzle along the plasma jet axis. On the left in the Figure 6 can be seen effect of the particle diameter on evaporation in the axial distance from the plasma jet [11].

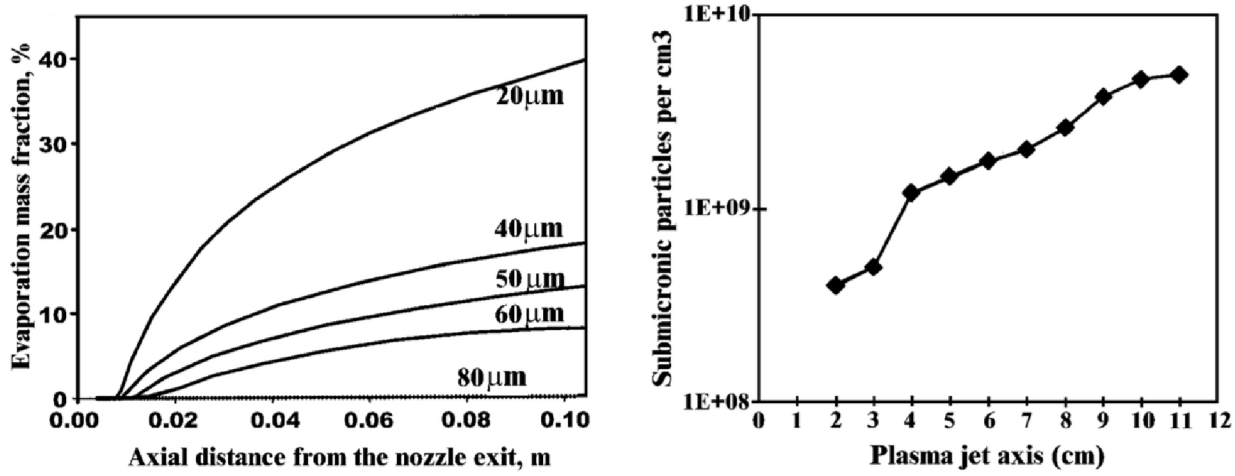


**Figure 6 - Left - Experimental data of evaporation mass fraction of different particle sizes with increasing axial distance from the nozzle exit. Right - Amount of submicronic particles with increasing axial distance [11]**

## Droplet Impact, Spread and Splat Formation

When a particle impacts the surface it flattens, spreads itself onto the substrate surface, solidifies and forms a splat, basic building block of thermal spray coating. The degree of flattening has been shown to be a power function of the Reynolds number as can be seen in the eq. 4 [9].

There are two basic modes in which the flattening of the incident particle can occur and those are: flattening and splashing. The temperature at which both mechanism are controlling the particle flattening is called transition temperature (Figure 7). Splashing is undesirable and results in higher porosity levels and overall lower adhesion

and cohesion [9]. To determine what mode of flattening will occur at impact of the particle onto the substrate, temperature needs to be taken into account and has been shown to be determined by eq. 5 and eq. 6 [9].

$$\frac{D}{d} = 1{,}29Re^{0{,}2} \tag{4}$$

$$K = We^{0{,}5}Re^{0{,}25} \tag{5}$$

$$K_f = 0{,}5a^{1{,}25}Re^{-0{,}3}K \tag{6}$$

Where $D$ is diameter of the splat and d is diameter of the original particle, Re is defined in the eq. 2, a is a ratio of the flattening velocity to the impact velocity of the particle, K is a flattening coefficient, $K_f$ is the splashing flattening coefficient and $K_{cf}$ is the critical splashing flattening coefficient. If $K_f$ value is higher than $K_{cf}$ (critical value for certain thermal spray setup) it is expected that splashing mode is the most dominant mode. This value corresponds to substrate transition temperature $T_t$ [9].

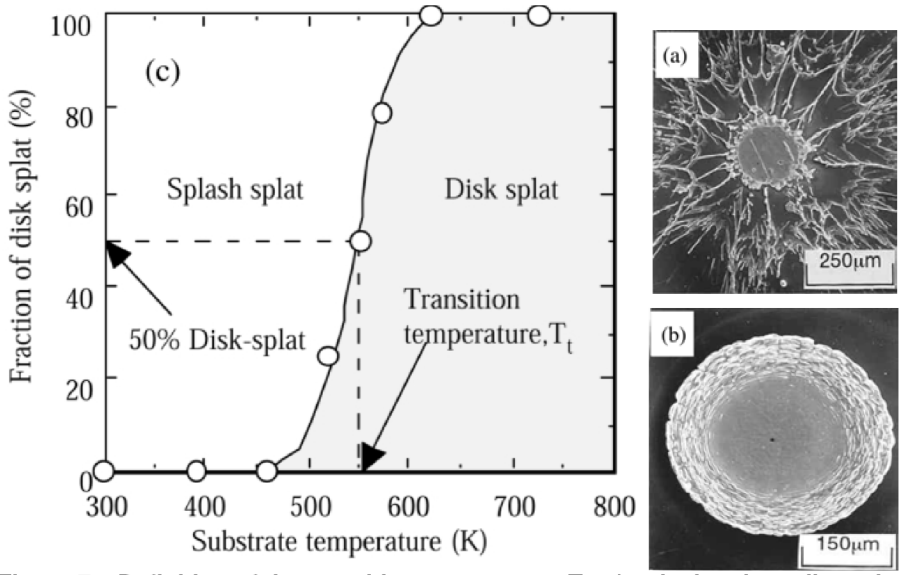


**Figure 7 – Definition of the transition temperature Tt. a) splash splat collected at Ts = 300 K. b) disk splat collected at Ts = 723 K [2]**

This is of course true only in the case the particle is fully melted. As for not fully melted particles there is not a complete theory on how they behave during spreading and solidification after impact. However it is expected that the unmelted part enhances the kinetic energy dissipation (slows the spreading process) and could also bounce away from the substrate and induce particle splashing. The result may be: high unmelted splat (Figure 8), low deposition efficiency and high coating porosity [8].

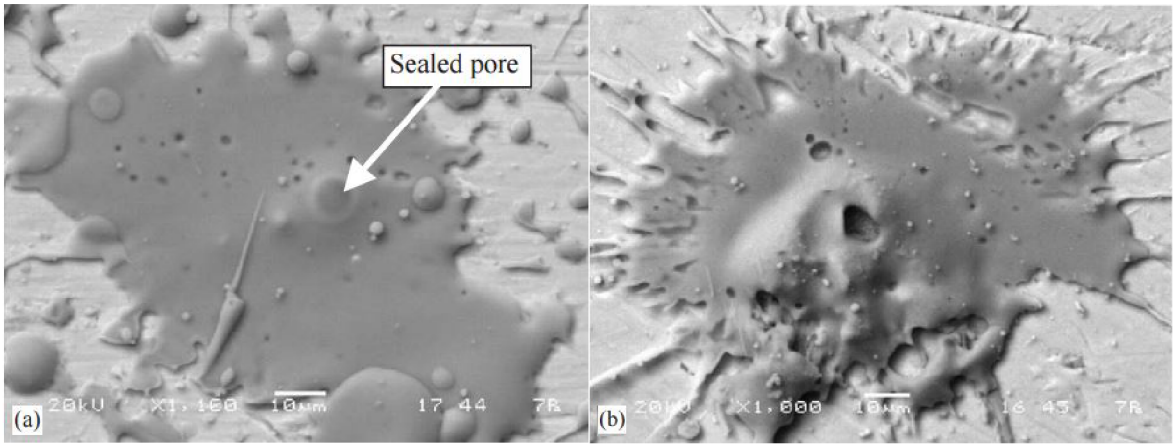


**Figure 8 - a) completely melted hydroxyapatite particle and b) partially melted hydroxyapatite particle [15]**

## Plasma Sprayed Coating Structure and Characteristics

The final coating is built from many individual splats typical coating structure is shown in the Figure 9. The microstructure contains porosity, cracks, inclusion, unmelted particles and oxides. Oxides that are present in the sprayed droplets flatten after impact with the substrate and can be observed generally as dark elongated phases in the coating microstructure. Oxide inclusions increase the coatings hardness [1, 5]. High oxide content result in brittle coatings and can lead to low cohesive strength. However, in certain cases it is desired to have certain amount of oxides present in the microstructure, as they can increase wear resistance and lower the thermal conductivity [1].

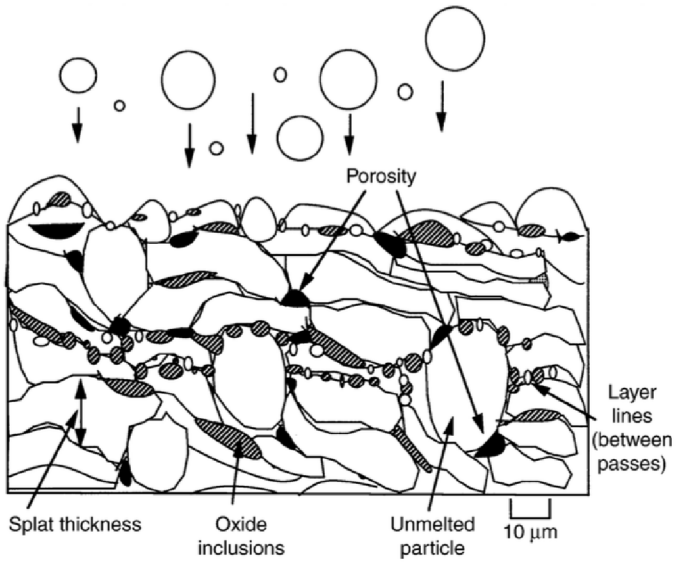


**Figure 9 - Schematically drawn microstructure of a plasma sprayed coating [1]**

Another important coating feature is porosity. It is generally associated with a high number of unmelted or resolidified particles that become trapped in the coating structure but can originate from all kind of different sources some those are for example [1]:

- Material shrinkage on cooling from the liquid state
- Separation of splats due to low cohesion

- Poor wetting onto adjacent surfaces (due to for example cool or slow moving particles)
- Intersplat or intrasplat cracking
- High deposition angles leading to shadowing

High porosity may result in poor coating adhesion and cohesion, premature cracking, delamination or spalling. It is especially undesirable in corrosion protection coatings as open porosity can short-circuit the corrosion resistance of the coating. It can also lead to poor surface finishes as non-uniform pits may form on the surface after grinding or honing porous coatings. Even though porosity does lower some coating properties it is sometimes desirable. In ceramic thermal barrier coatings low heat conductivity can further be lowered by inclusion of 8-15% porosity. Porosity can also serve as a reservoir for oil/grease or solid-lubricant in bearings, or in biomedical applications porous coatings can provide a structure that osteoblastic cells can grow into [1].

## 2.1.5. Adhesion Mechanisms

The ability of the coating to stick to the substrate depends on several types of mechanisms. The adhesion mechanism is still not fully understood however it is expected that both mechanical anchorage and physical-metallurgical adhesion occur [12].

### Physical Adherence

According to a theory proposed by Zaat, the main conditions for physical adherence are [13]:

- Intensive and permanent contact between substrate and lamella
- Decrease in the Gibbs free energy of the substrate and lamella system
- Very clean surfaces

If two very clean surfaces without any mechanical stress approach each other to the field of attraction (i.e. smaller than 5 Å), the Gibbs free energy of the atoms decreases and leads to enhanced adhesion. The Gibbs free energy of the atoms has to be increased again to separate the two surfaces and this according to the second law of thermodynamics, cannot happen without overcoming certain energy barrier first. The total decrease of the Gibbs free energy is given by [13, 14]:

$$\Delta G = \Delta G_{surf} - T_{cont}\Delta S_s + \Delta H_s \qquad (7)$$

Where $\Delta G_{surf}$ is a decrease of the Gibbs free energy due to surface energy, $T_{cont}$ is the contact temperature, $\Delta S_S$ is increase of the entropy due to surface diffusion and $\Delta H_S$ is a change of the enthalpy because of different potential curves for atoms combinations AA, BB and AB (A – substrate atoms, B – coating atoms). In the equation mechanical aspects like the residual stresses are not taken into account. In practice this decrease of the Gibbs free energy happens only in places where the contact between the coating layer and the substrate is close enough for surface atoms to reach the field of attraction. Therefore better and longer liquefied state of the sprayed material increases the probability for a better adherence [13].

### Mechanical Anchorage and Thermal Mechanisms

Generally, mechanical anchorage is believed to have the biggest impact on the adhesion of the coating. This is especially true for ceramic and other high melting point materials where metallurgical or chemical reactions with the substrate during deposition are not expected. For good mechanical anchorage, it is important that the surface of the substrate is properly activated. This is achieved by a proper cleaning of the surface, proper surface roughness and substrate preheating [15, 16]. Mechanical anchorage is the result of residual stresses induced in the coating during rapid solidification of splats. However thermal expansion of both substrate and coating material have to be taken into account as mismatch in these values could reduce the effect residual stresses have on the adhesion [16].

Preheating of the substrate is another important factor that influences adhesion. Wetting of the impacted particle is increased, the heat convection into the substrate is not as rapid and the particle remains in the molten state longer [15, 16]. Impacted particles may cause substrate melting resulting in formation of an alloy layer which exhibits superior adhesion strength when compared to mechanical anchorage. Substrate melting is only possible for certain material combinations. Generally if the melting point of the sprayed material is higher than that of the substrate, formation of an alloy layer could be expected if substrate is preheated enough [13]. Preheating also ensures burning off any residual greases, oils and moisture present at the substrate surface and has a positive effect on residual stresses in the coating [13].

## 2.2. Materials

### 2.2.1. Thermal Barrier Coatings (TBC)

The gas turbine engines provide for one of the most challenging environments that material systems have to deal with today. Engine components are under enormous mechanical loading conditions (high temperatures, corrosive and erosive media, etc.) [17]. The best way to increase the efficiency of an engine is to increase the combustion temperature. Therefore advances in thermal spray technology led to the use of TBC coatings. These coatings are heat and oxidation resistant and protect the substrate from exposure to high thermal loads due to its low heat conductivity and thus allow for higher combustion temperatures [17]. TBC structure can be seen in the Figure 10.

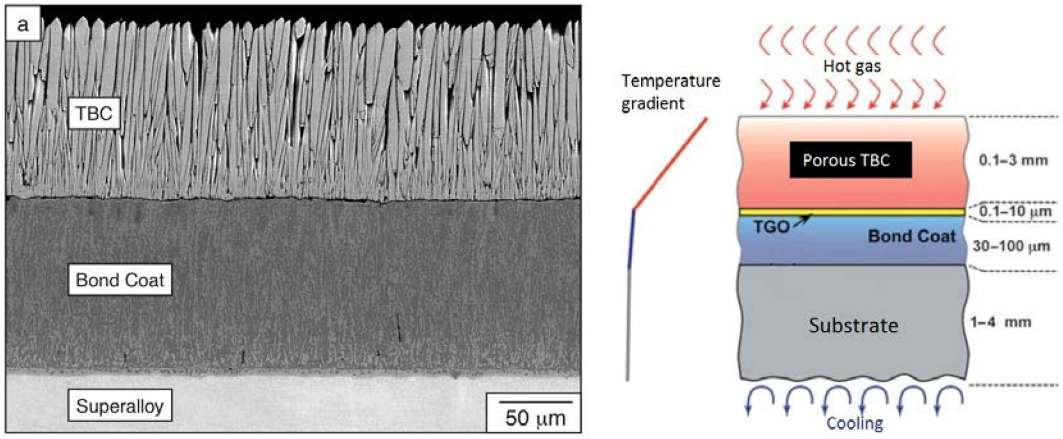


**Figure 10 – Left – Microstructure of TBC system [20]. Right – Schematically drawn TBC system [3]**

Most common industrially used TBC coating system has been so far plasma sprayed $ZrO_2$ - (6-8 wt. %) $Y_2O_3$ ceramic layer (also referred to as YSZ) over a MCrAlY (M = mainly Ni, Co) bond coat layer [18].

#### YSZ Top Coat

There is a wide selection of ceramic materials that could be used in TBC coatings. The reasons yttrium stabilized zirconia is so popular choice are its superior mechanical properties such as high strength and fracture toughness combined with wear resistance and on top of that it also has a thermal expansion coefficient close to that of metallic substrates as can be seen in the Figure 12 [19]. ZrO2 exists in three crystallographic phases (Figure 11): low-temperature monoclinic phase, the intermediate-temperature tetragonal phase and the high-temperature cubic phase. The drawback is that the phase transformation of tetragonal to monoclinic phase is accompanied by significant volume expansion (approximately 3-5 vol.%). This transition induces stresses on the coating/substrate interface and generally contributes to the failure of the TBC system. Therefore, the amount of monoclinic phase in ZrO2 is one of the important indicators of coating quality [20].

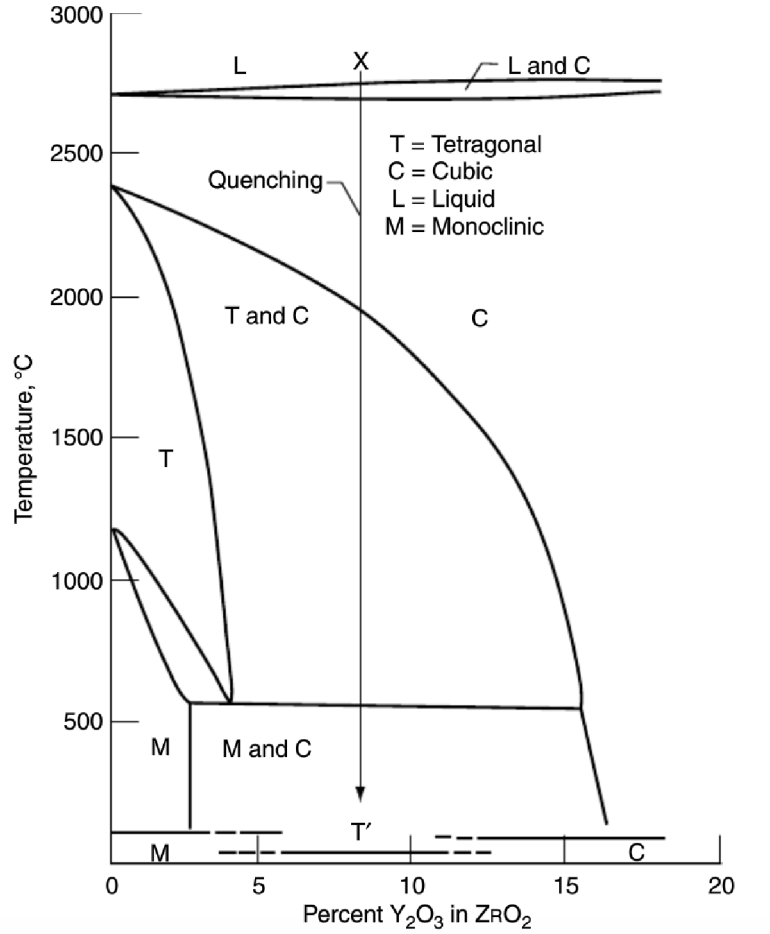


**Figure 11 - Phase diagram of $ZrO_2$ – $Y_2O_3$ system [21]**

To minimize the effect of volume expansion several oxides can be added (Y2O3, CeO2, MgO). These can stabilize the high-temperature cubic phase and repress the existence of the unwanted monoclinic phase. In the case of YSZ, rapid solidification during the plasma spray process can drive diffusionless transformation from the high-temperature cubic phase to the non-transformable tetragonal phase without a composition change [22]. The non-transformable tetragonal phase is unstable with respect to diffusion at high temperatures. Therefore, additional phase transformation into the equilibrium high-yttria cubic and low-yttria tetragonal phases can be expected on high-temperature exposure. The phase transformation is additionally affected by various conditions, such as aging and cooling rate [20].

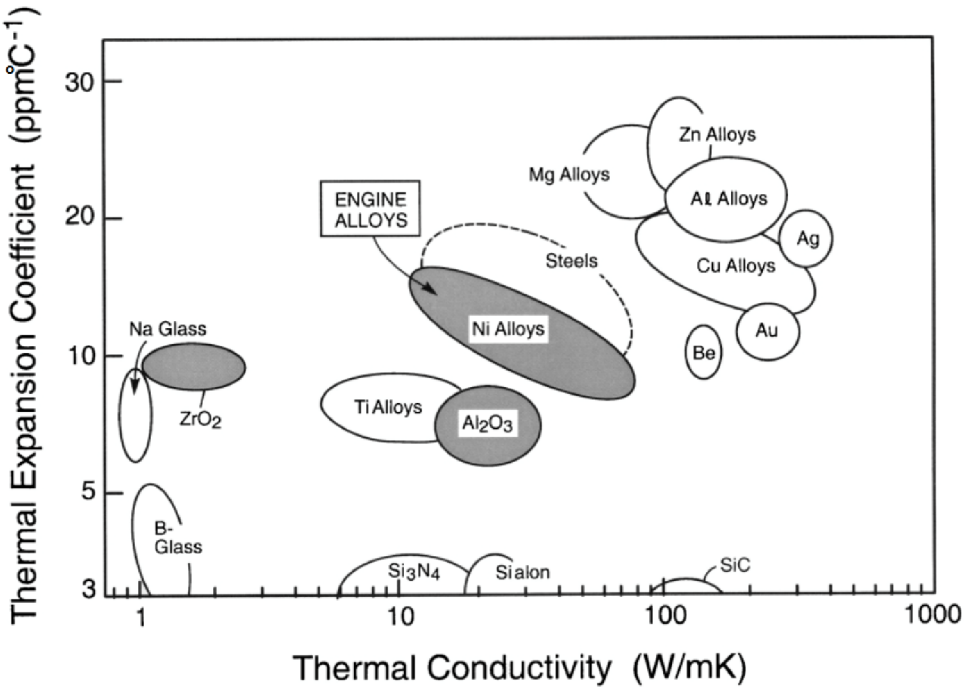


**Figure 12 - Diagram of thermal expansion coefficient versus thermal conductivity for different materials [23]**

## MCrAlY Bond Coats

As a bond coat for the TBC topcoat the most commonly used are the MCrAlY type coatings. Their composition is similar to that of superalloys that are being used for components working at high temperatures, so the coating is inherently resistant to elevated temperatures. Microstructure of MCrAlY coatings as with many other alloys is largely dependent on its composition and operating temperature. The phases present in the microstructure during its service life are (see Figure 13 for lattice structure of the most common phases) [19]:

- β - Has BCC lattice and contains (Co, Ni)Al
- γ - Has a FCC lattice and is a solid solution of Co, Ni, Cr
- γ ` - $Ni_3Al$ intermetallic phase
- Other – other phases that may be present depending on the composition of the bond coat and are σ – brittle phase and α phase which is high in chromium content. Both of these phases are undesirable

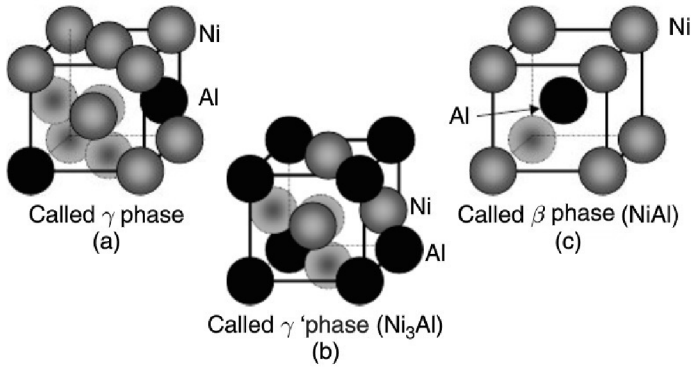


**Figure 13 - Lattice structures of the most common phases present in MCrAlY coatings [19]**

The most common phase combinations are γ+β (the most desired) or γ+β+others [19]. The β phase has NiAl chemistry in which other elements like Co and Cr can dissolve [24]. Co forms beta phase preferentially and can even replace Ni entirely [19]. Cr shows no special preference on Ni and Al sites in the β phase, but usually occupies the sites on which the element (Ni or Al) is poorer in content [24]. Cr usually has a higher solubility in γ phase than in β phase [19]. Ternary diagrams of Ni-Cr-Al are well known and are presented in the Figure 14. When other elements like Co or Re are added however, the diagrams get very complicated [25].

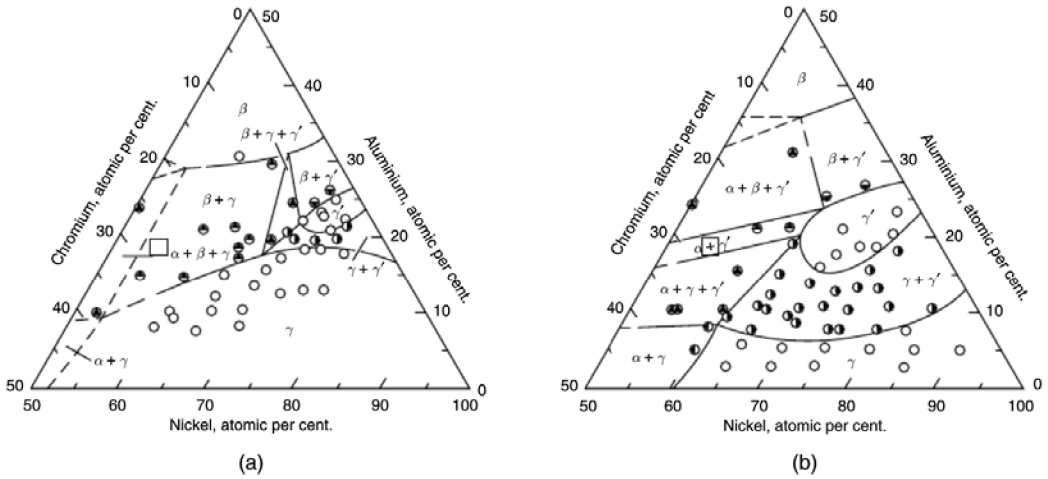


**Figure 14 - Phase diagrams for Ni-Cr-Al at elevated temperatures. a) for 1422 K and b) for 1122 K [24]**

As can be seen from Figure 14, phase transformations take place as the temperature increases. One of the most undesired transformations is γ+β=α+γ` which is accompanied by significant volume expansion and induces large stresses in the coating [24].

## Bondcoat/Substrate Diffusion

At high service temperatures negative diffusion processes occur (up to 1272 K) at the bond coat/substrate interface. These processes mainly occur due to large differences in chemical activity between the coating and the substrate material [25]. Ni-base superalloys contain a number of alloying elements such as Co, Re, W, Nb, Ti, ect. mainly to improve the high temperature mechanical properties. However, MCrAlY-type bond coats are rich in elements like Al and Cr to promote the formation of a protective oxide scale. This compositional difference acts as the driving force for the inter diffusion between the substrate and the coating. As a result, microstructural changes near the and at the coating/alloy interface are generated both in the substrate and in the coating. This inter diffusion can lead to the formation of detrimental phases, such as sigma-phase, Laves phases, brittle carbides and other coating imperfections like voids and porosity [25]. This leads to changes in the mechanical properties of the substrate and can eventually lead to failure [26, 28] [26].

## Thermally Grown Oxide (TGO)

When the MCrAlY bond coat is exposed to high temperatures, oxide layer forms at the bond coat/topcoat interface (see Figure 15). This layer acts as a barrier to oxidizing elements that penetrate through the porous topcoat. The TGO is mainly formed by

α-$Al_2O_3$ and even though the growth phenomena in the TBC system is not quite quantitatively comprehended, the following findings are accepted as applicable [23]:

The growth is essentially parabolic until spallation occurs. The growth rate is given by equation 9 [23]:

$$h^2 = 2k_p t \tag{8}$$

Where $h$ is thickness of TGO, $t$ stands for time and $k_p$ is the parabolic rate constant. This process is controlled by diffusion. In some cases Θ-alumina forms first and transforms to α-$Al_2O_3$ [19]. Small amount of Cr and Ni oxides may also form first because of higher diffusivity of these elements. Mechanism of the TGO growth is a diffusion of oxygen either directly from $ZrO_2$ lattice or by oxygen penetration from surrounding atmosphere through the topcoat porous structure. The mechanism of TGO growth is therefore controlled by diffusion. As a source of Al serves the β phase. After high temperature exposure depletion of this phase occurs and after a period of time depleted β phase zone becomes noticeable in the bond coat microstructure. During the service time, due to stresses induced by the TGO growth, the oxide layer spallation and cracking may occur. TGO is continuously being renewed, however after depletion of the β phase becomes significant, the renewal stops and leads to failure of the bond coat [26].

The adhesion of TGO is crucial to the bond coat lifetime. To increase this ability of adherence reactive elements such as yttrium or rhenium are added. Several mechanisms that are responsible for the adhesion increase have been proposed and most of them focus on modification of Al transport in the alloy. Those mechanisms are so called "pegging" of the coating by oxides of these reactive elements form or by altering of growth and TGO plasticity [29].

Apart from α-$Al_2O_3$ other oxides like $Cr_2O_3$ CoO and NiO may form as well as spinel oxides (e.g. (Co, Ni)(Cr, Al)$_2O_4$) at high temperatures and long exposure times. This is also a point where failure may occur because these oxides and especially spinels promote spallation [26, 27].

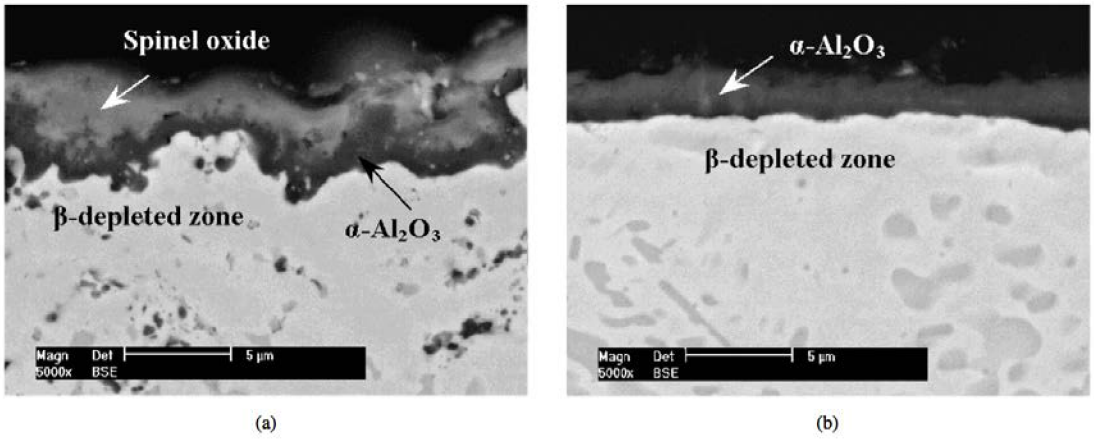


**Figure 15 - MCrAlY coating after high temperature exposure. a) Highlighted formed spinel oxide on top of TGO and β depleted zone. b) Highlighted alumina TGO and β depleted zone [27]**

## 2.3. Electron Beam

Recently the technology of high power density heat sources such as electron and laser beams has gone through a rapid development and is being applied in welding, cutting, surface heat treating and alloying. Electron beam technology used for these purposes is very similar to the technology used in electron microscopes, but the energy density in this case is much higher [30].

### 2.3.1. EB System Design

Typical EB machine is schematically represented in Figure 16. The main components of EB machine are: the beam generator, the beam forming and guiding sections (which has separate vacuum system) and a vacuum chamber [31]. The EB interacts with the surrounding atmosphere and this causes its scattering and a loss in its energy density. Vacuum is needed to minimize this effect [32].

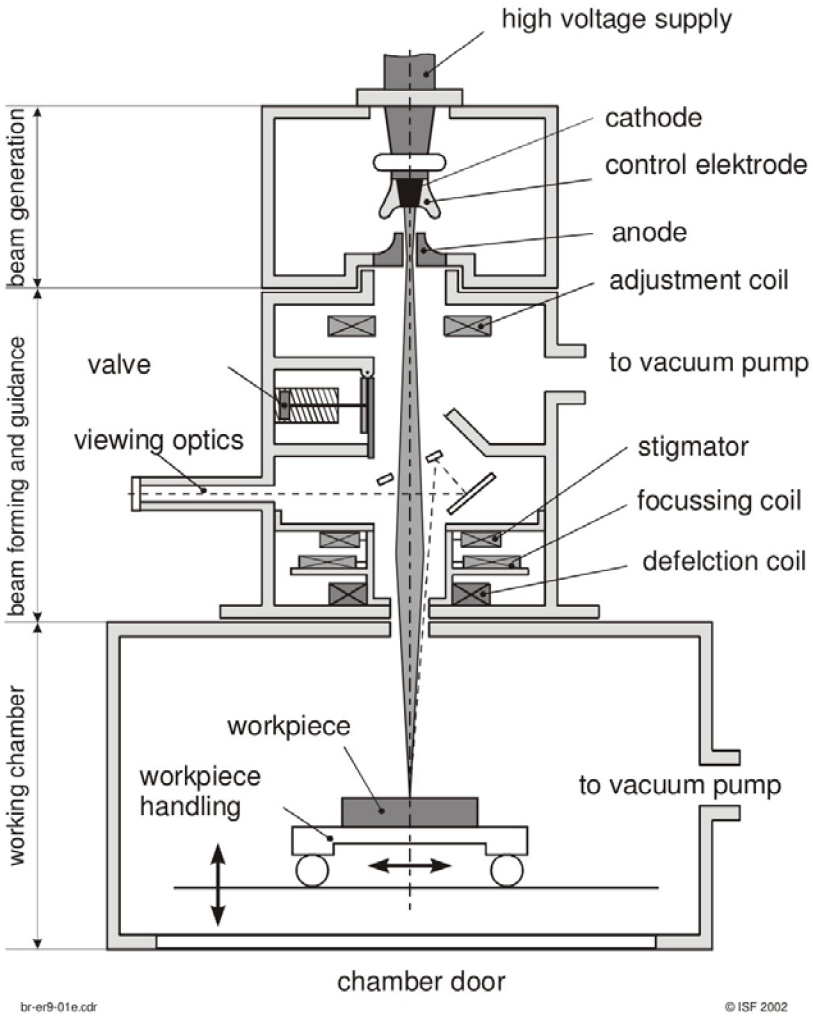


**Figure 16 - Schematic representation of electron beam device [36]**

### 2.3.2. EB Generator

A tungsten cathode, which has been heated under vacuum, emits electrons by thermal emission. The electrons are accelerated by high voltage between the cathode and the pierced anode (see Figure 16). A modulating electrode called “Wehnelt cylinder”, which is positioned between anode and cathode, regulates the electron flow. Dependent on the height of the cut-off voltage between the cathode and the modulating electrode, is a barrier field, which may pass only a certain quantity of electrons. This happens during an electron excess in front of the cathode where it culminates in a form of an electron cloud [31].

### 2.3.3. Beam Manipulation and Formation

Because electrons of which the EB consists have an electric charge, the beam can be easily manipulated by magnetic fields. The beam starts to diverge after it emerges from the aperture in the anode because of mutual repulsion and other effects [31].

The beam is guided through a system of alignment and focusing coils onto the workpiece (stigmator coil may be added to correct aberrations of the lenses). Deflection coils below the system of focusing coils cause the beam to move to predetermined locations and it is focused to a spot of a diameter in the range of 0,1 - 1 mm. The coil is also being used to split the beam, allowing to combine multiple processes together [31].

### 2.3.4. Working Chamber

The working chamber is evacuated and must be capable of withstanding the air pressure, which acts on the walls of the chamber. Usually, regular structural steel is used that significantly reduces the interfering effects of external magnetic fields. The chamber must also be equipped with appropriate positioning equipment for the workpiece. When in operation, especially while using high energy EB, a layer of metal condensate is continuously deposited on the surface of the internal walls of the chamber. For this reason metal plates can be mounted onto the internal walls of the chamber to simplify the cleaning process of the chamber [31].

## 2.4. EB Interaction With Material

The electron beam interacts with the material atoms and becomes significantly scattered through elastic (trajectory of electrons changes, but its kinetic energy and velocity remain essentially constant) [33] and inelastic (interactions with the material trajectory of incident electron is only slightly changed, but its energy is lost through interactions with orbital electrons of the atoms in the substrate) [33]. Inelastic interactions produce diverse effects including (see Figure 17):

- Emission of secondary electrons
- Phonon excitation
- Emission of characteristic x-ray radiation
- Plasmon production
- Auger electron emission

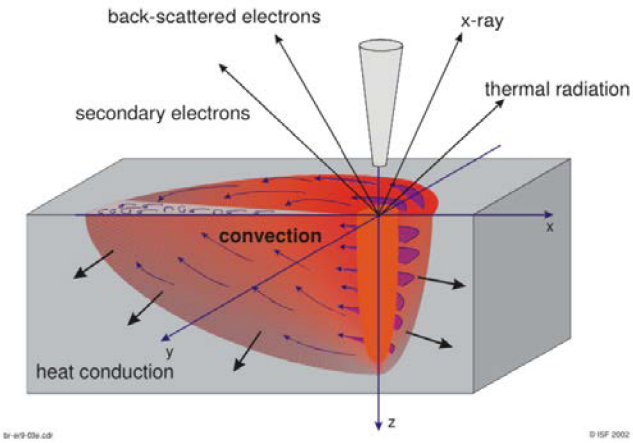


**Figure 17 - Effects of interaction of EB with the substrate [36]**

Unlike in electron microscopy where most of the above mentioned effects are important, when using EB for surface treatment of the workpiece, the most important interaction is the phonon excitation of the workpiece atom lattice (although backscattered electrons can be used to monitor the process) [34], because that's how most of the EB kinetic energy is transferred into the workpiece. Phonon excitation macroscopically results in an increased temperature of the incident workpiece volume. Outcome of the EB interaction with the workpiece can be separated accordingly (with respect to the beam energy):

$$E_1 < E_2 < E_3 < E_4 \tag{9}$$

- $E_1$ - the workpiece is heated but remains solid without undergoing any phase transformation
- $E_2$ - the heated substrate remains solid and phase transformation takes place
- $E_3$ - the substrate is heated above its liquidus temperature into a liquid phase (alloying, surface remelting)
- $E_4$ - the substrate is heated up to its vapor phase

### 2.4.1. EB Surface Heating and Hardening

First category of EB treatments can be used for are heating and hardening of metals. These treatments can eventually be combined with tempering to reduce induced stresses by rapid heating of the surface layer as can be seen in the Figure 18 [37]. This is done with the help of the deflection coil. For these kinds of treatments lower energies are used (energies corresponding to $E_1$, $E_2$ as described in chapter 2.4). The substrate in this case remains in a solid state. EB surface hardening is a process that uses the heat generated by the impingement of an electron beam on the surface of the material to austenitize it, and then the austenitized layers are transformed to martensite because of a rapid conduction of heat into the cold interior of the workpiece [36]. This effect is known as self-quenching and the cooling rates are usually high enough to allow martensite formation, even in steels, which have a low hardening ability [37]. In addition the hardened microstructure obtained is usually finer than that from a conventional heat treatment, resulting in hardness and consequently fatigue resistance increase [38]. The thickness of such hardened layers usually varies from 0,1 to 1,7 mm [31].

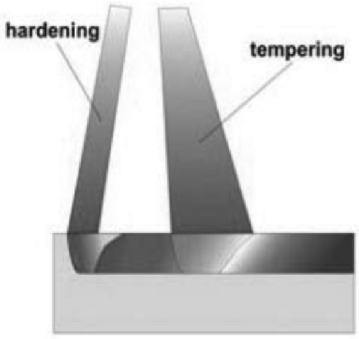


**Figure 18 - Combination of EB surface hardening and tempering [37]**

## 2.4.2. EB Surface Remelting, Alloying and Dispersion

Another category of EB operations are surface remelting and alloying, where higher energies are used (corresponding to $E_3$ as described in chapter 2.4). Remelting the substrate surface alone by the high energy EB generally results in a finer grain structure of the material and can result in higher wear resistance and increased hardness. In some cases the rapid solidification can result in amorphous structure of the remelted surface layer [32]. The thickness of remelted layer ranges from 0.1 to 10 mm [31].

If a layer of certain element or alloy is applied onto the surface of the substrate (for example by a thermal spray technology, thin foil or vapor deposition) and subsequently the layer is remelted, it leads to mixing of the coating layer with the base material. Assuming that the beam penetration depth is larger than the thickness of the applied layer. This process is called alloying and creates a surface with properties that differ from those of the base material. Another process EB surface remelting is used for is called dispersion. This occurs when the material deposited onto the base material does not melt and it is dispersed into the substrate surface. Alloying suitable elements into the substrates surface results in better surface properties, like wear and corrosion resistance [31].

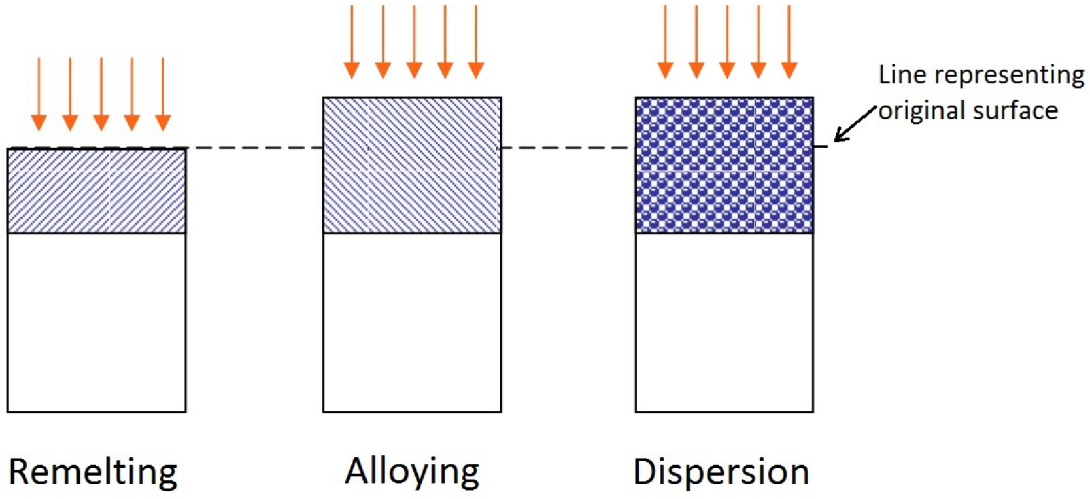


**Figure 19 - Schematic picture of different processes in the liquid phase EB is used for [35]**

### 2.4.3. EB Welding

When EB with high enough energy (corresponding to $E_4$) interacts with a substrate, the substrate material evaporates and allows the following electrons a deeper penetration. The result is a formation of a vapor cavity surrounded by a shell of fluid metal also called a keyhole. The diameter of the cavity approximately corresponds to the beam diameter [31].

To maintain the keyhole stability the vapor pressure must press the molten metal round the vapor column against the cavity walls, by counteracting its hydrostatic pressure and surface tension (see Figure 20) [31]. As the beam traverses over the base metal, the material melts at the leading edge of the keyhole, flows around the keyhole, and solidifies at the trailing edge (see Figure 20) [32]. This leads to continuous collapse and formation of the keyhole and formation of the weld. This type of welding can however result in cold shuts, porosity, or irregular penetration. These defects are to some extent corrected by modern beam power input control techniques [31]. Heat affected zone is narrow and depending on the material the EB is able to weld workpieces with up to 500 mm (aluminum) in thickness. There is no need for additional material to form the weld and welding speeds are considerably higher compared to conventional methods [31].

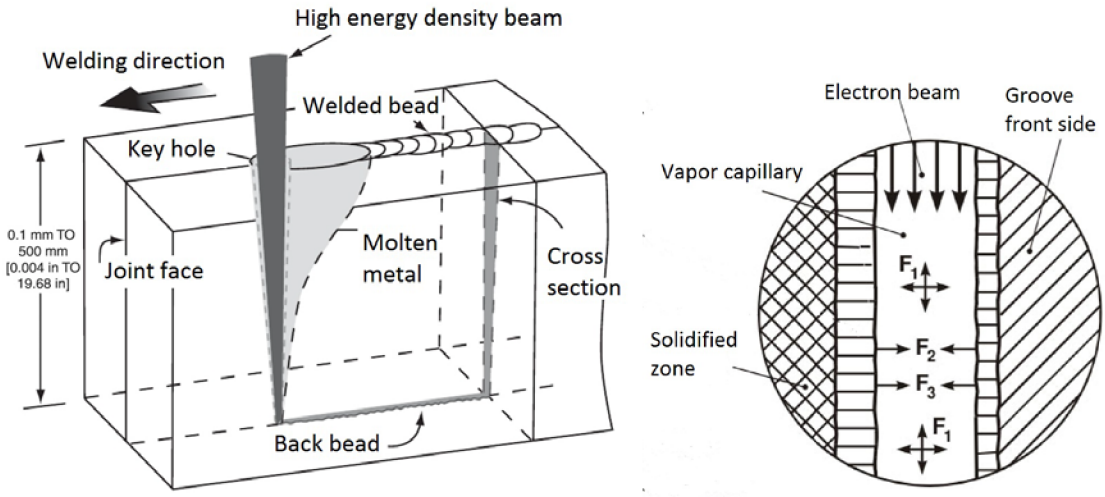


**Figure 20 – Left - Schematic representation of the welding process [32]. Right - forces acting inside the keyhole [32].**

# 3. Experimental Setup and Equipment

## 3.1. Materials

### 3.1.1. NiCrAlY Powder

Manufacturer of powder used for purposes of this work was H.C. Starck. The product name is Amperit 413 NiCrAlY and was made by gas atomization method. The powder was supplied by the Institute of Plasma Physics in Prague. The powder was analyzed using SEM, EDX, XDR and particle size analysis. Particles of the powder have relatively regular sphere shaped morphology which corresponds to the gas atomization method used for manufacturing. The particle bodies have attached node shaped satellites, as could be seen from Figure 21.

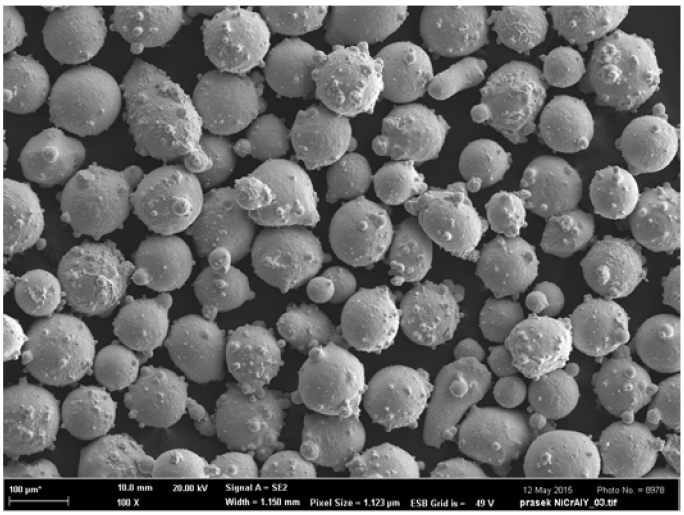


**Figure 21 - Morphology of the used NiCrAlY powder**

The particle size distribution was measured by laser diffraction method using Mastersizer 3000 device made by Malvern. This device allows using either wet or dry dispersion type and is able to measure size distributions in the range of 0.01 µm to 3500 µm. Wet dispersion was used when carrying out the measurement, results of the measurement are presented in Figure 22. The distribution of the average particle size is following: D10: 49,0 µm; D50: 81,7 µm; D90: 137,0 µm**.** According to the information provided by the manufacturer the powder is suitable for deposition by APS, HVOF and VPS methods. The chemical composition from EDX can be seen in Table 2. Phase composition data acquired from the XDR analysis are in the Figure 23. The most dominant phase (67 %) in the powder microstructure is γ – Ni(Cr) which is a solid solution of Ni and second phase present is intermetallic phase NiAl (33 %).

**Table 2 - Results from EDX mapping analysis of the NiCrAlY powder (in wt. %)**

| Ni | Cr | Al | Y |
|---|---|---|---|
| 66,1 | 23,9 | 9,0 | 1,0 |

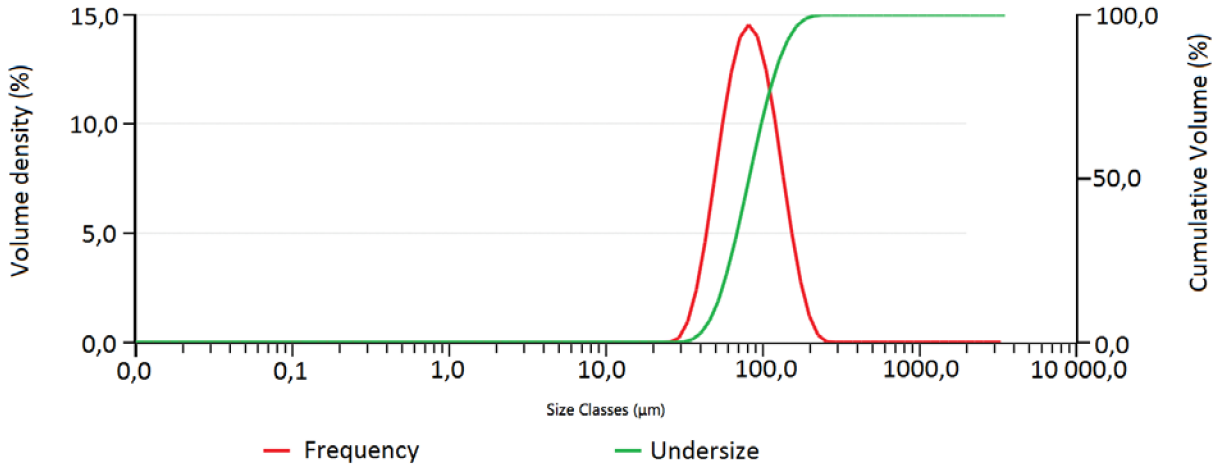


**Figure 22 - Particle size distribution of the used NiCrAlY powder**

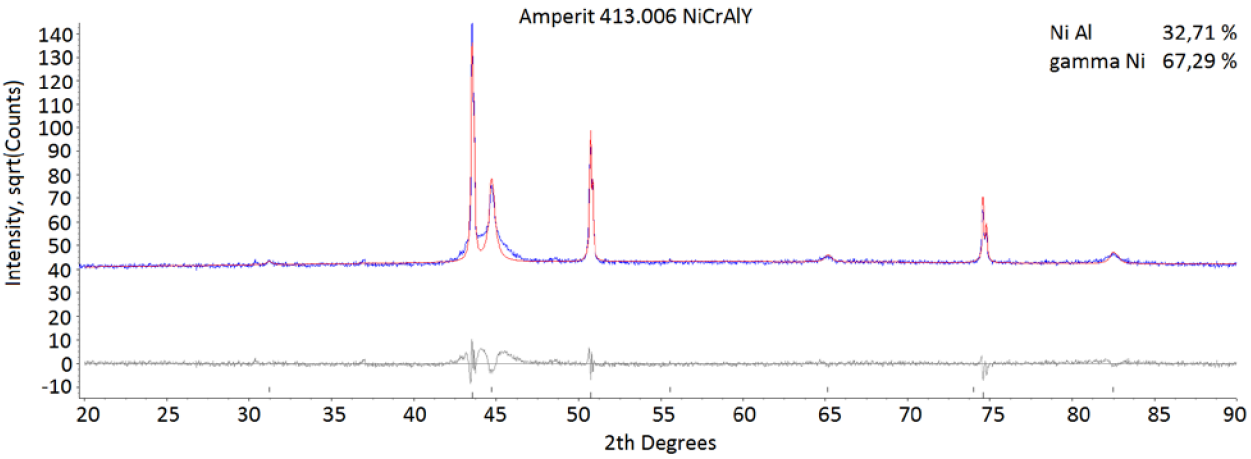


**Figure 23 - XDR analysis of NiCrAlY powder**

## 3.1.2. Substrate Geometry and Material

Material used for the substrate was grade 11 steel S235JRC+C. Chemical composition of the substrate material is in Table 3. The substrates were manufactured at FSI VUT Brno with guidelines provided by ASTM C-633, EN 582 standard for tensile strength adhesion testing. The substrate blueprint can be seen in the Figure 24.

**Table 3 - Chemical composition of the substrate (in wt. %)**

| C | Mn | P | S | N | Fe |
|---|---|---|---|---|---|
| max 0,21 | max 1,50 | max 0,055 | max 0,055 | max 0,011 | balance |

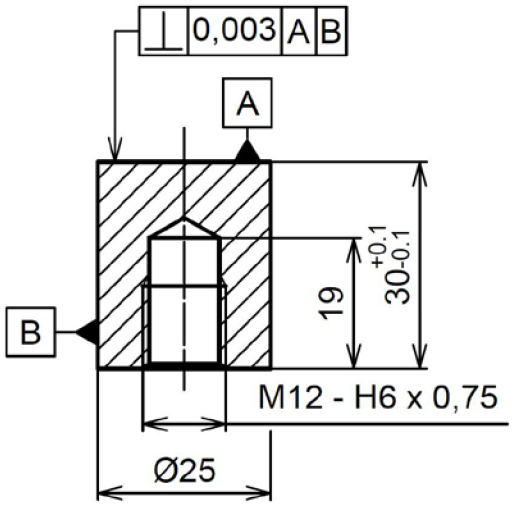


**Figure 24 - Scheme of the substrate used for deposition**

### 3.1.3. Water Stabilized Plasma Spray Deposition

NiCrAlY coatings were deposited in Prague at the Institute of Plasma Physics using water stabilized plasma technology. Due to intellectual property of the project partner, the exact deposition parameters will not be disclosed. Further to that, it is important to note that **the used parameters and overall spraying conditions were not optimized** and therefore the coating properties may not be ideal, mainly because of expected oxide content.

### 3.1.4. Coating Deposition

Prior to the deposition, the substrates were grit blasted with corundum and degreased in acetone. The substrates were mounted on a revolving carousel, which was turning at 2 rps (revolutions per second) to ensure uniform spraying. The samples were being cooled by argon gas during the deposition (see Figure 26). The deposited coating had a metallic coloration and layer of green colored oxides in the form of dust layer was present in the “out-of-sight” places as can be seen in the Figure 27.

The temperature of the samples was monitored by a wireless thermocouple attached to the back of one of the samples. Thermal history of the monitored sample can be seen in Figure 25:

- Preheat: 3 passes to about 150°C (no powder feeding)
- Spraying: two deposition cycles; 2 passes up and 3 passes down in each cycle
- Maximum temperature at the back of the monitored sample was below 180°C. See Figure 27 for the wireless thermocouple position.
- Feed rate: 13 $kg.hour^{-1}$
- Torch vertical speed: 50 $mm.sec^{-1}$
- Carousel rotation speed: 2 rps

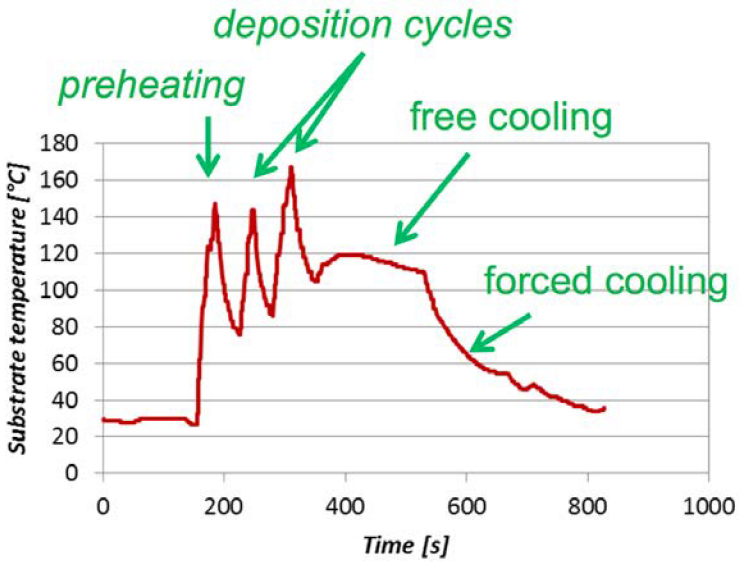


**Figure 25 - Thermal history of a sample monitored by a thermocouple during NiCrAlY plasma deposition**

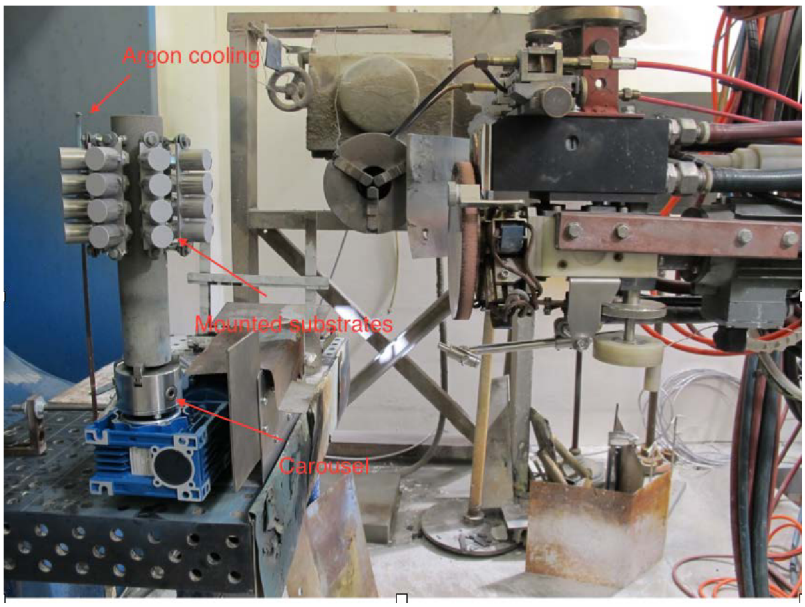


**Figure 26 - Deposition setup**

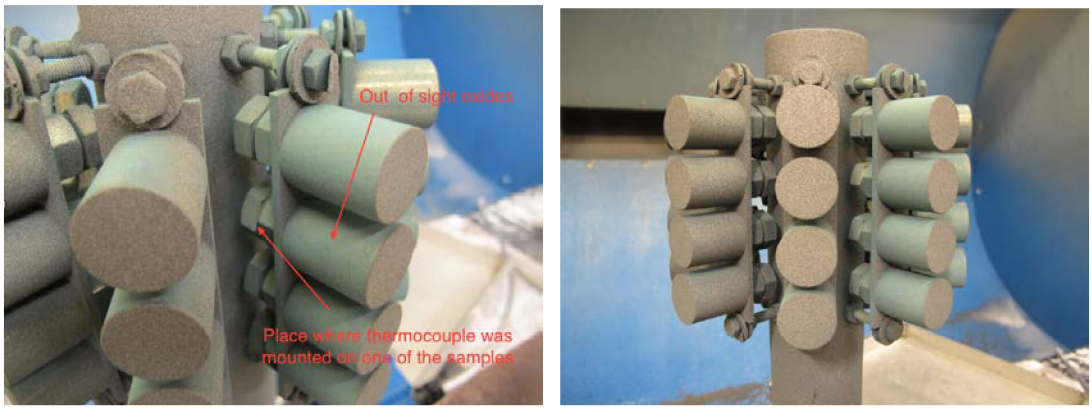


**Figure 27 – Samples after the deposition**

### 3.1.5. In Flight Monitoring

The in-flight particle properties were measured by DPV-2000 system. This system helps to determine the characteristics of spray particles during the flight phase in a specific area of the spray jet. The surface temperature (two-wavelength pyrometry), the flux amount, the particle diameter (iterative, manual adjustment of the emission coefficients) and the speed of the spray particles (light barrier principle) can all be measured simultaneously. The results of the measurement were the following:

- Mean particles temperature: 2535 ± 89°C
- Mean particles velocity: 45,3 ± 5,0 $m.s^{-1}$
- Mean particles diameter: 79,3 ± 12,8 μm

The particle was well above the melting temperature but the velocity was rather slow when compared to regular velocities achieved during WSP spraying (in hundreds $mms^{-1}$) [2].

## 3.2. Electron Beam (EB) Modification

EB surface remelting has been chosen as a method to modify the coating/substrate interface. The type of the machine used was K26 made by German company Pro-beam. This device was acquired under the project NETME. This device has a vacuum chamber with a multi-axis platform with numerical control positioning system and a electron gun. Included are also bushings for supply of inert gasses and cooling water. This device can be used for welding regular and reactive metals and for heat treatment including quenching, surface remelting and alloying of surface layers.

### 3.2.1. Optimization of EB Parameters

Modification of thermally sprayed layers is a novel research at VUT FSI in Brno and is being explored by this institution. For this reason it has been decided to gradually try several optimization steps. After evaluation of each result, 2 most promising sets of parameters were chosen and used to modify specimens that were later be used for adhesion testing. The electron beam was set to oscillate to form a 30 mm long line pattern to ensure even distribution of the heat energy input into the specimens. The parameters that were being optimized and its expected influence on final structure were the following:

- **Oscillation frequency** – better uniformity of the final surface with increasing frequency
- **Power input** – depth of the modified zone increasing with higher power input
- **Velocity of the beam shifting** – the higher the speed the lower the heat input into the specimen and lower depth of the modified zone

After a successful modification of the substrate/coating interface, dark phases formed on the surface. After several optimization steps it was assumed that it was most likely not possible to suppress formation of this phase. Focus was then directed only on the quality of the modified interface and after evaluation of the microstructures of each specimen 2 most promising sets of parameters were selected for final sets preparation.

### 3.2.2. Final EB modifications

The parameters chosen for modification of the final two series (B and C series; A series being the substrates in as-sprayed condition) can be seen in the Table 4.

**Table 4 - Parameters chosen for final modifications**

| Series | Velocity | Current | Voltage | Power Input |
|---|---|---|---|---|
| | [mm.s$^{-1}$] | [mA] | [kV] | [W] |
| Series B | 10 | 25 | 120 | 3000 |
| Series C | 5 | 18 | 120 | 2160 |

However when modifying specimen from series B and C, the results were different from those achieved during optimization. First problem was that the dark phase (that formed only in some places on the surface during optimization) now formed a consistent layer covering the whole surface of the specimen. Second complication was a geometry of the modified surface. This was most likely caused by migration of the material when in the liquid phase due to convective phenomena. Each specimen was therefore grinded using abrasive papers of a grit size 800 and 1200 for 3 minutes for each paper. It did not result in removal of the oxide surface layer but it did even up the surface. After this preparation series of tests of specimens from series B were carried out to test the adhesive strength of the oxide layer.

After the adhesion test of the oxide layer grinding was done on a magnetic grinder to achieve planar like surface. The profile of the reference specimen in each series was analyzed using light microscopy to determine how much material can be grinded away to get plane like geometry of the surface while the modified layer still stays intact. Series B before and after grinding can be seen in the Figure 28.

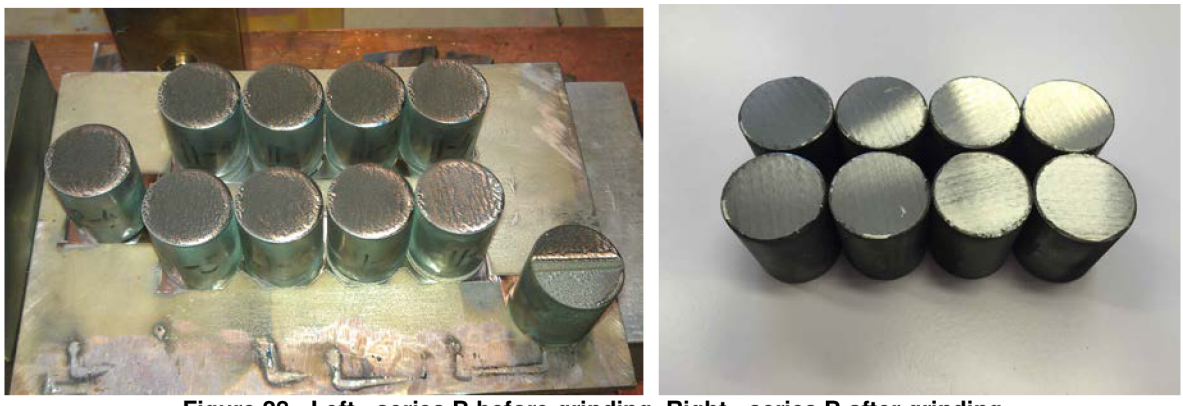

**Figure 28 - Left - series B before grinding. Right - series B after grinding**

## 3.3. Adhesion Testing

Adhesion tests were carried out according to guidelines provided by ASTM C-633, EN 582) standard [39, 40]. The method serves for determination of the degree of bonding strength of a coating to a substrate or the cohesive strength of the coating in a tension normal to the substrate. The test consists of coating one face of a substrate fixture, bonding this coating to the face of a loading fixture, and subjecting this assembly to a tensile load normal to the plane of the coating. This method is particularly adapted for testing of thermally sprayed coatings. Ambient temperature is the most suitable for

performing the tests. In case of using different temperatures the operating temperature of the bonding agent has to be taken into account.

The minimum recommended thickness of the tested coating is 0,38 mm. This limitation is imposed because the adhesive bonding agent is used and in some cases it is possible for the agent to penetrate through the coating, get in contact with the substrate surface and invalidate the results. However if the coating is dense enough or the bonding agent has high surface tension (eliminating the danger of the bonding agent leaking through the coating) coatings with lower thickness may be used.

The values of adhesive/cohesive strength of thermal spray coatings obtained by this method should not be considered for a direct use in making calculations, e.g. to determine whether a coating will withstand specific environmental stresses. It has to be kept in mind that because of residual stresses, the actual adhesive strength strongly depends on the shape of the particular coated part.

### 3.3.1. Setup

The coating was applied on a base of one fixture and then bonded with a base of another fixture using adhesive agent, the setup for the testing is represented in the Figure 29. The tests were carried out using a Zwick Z250 Allround-Line, tCII**.** According to the standard, the constant rate of the cross-head travel should be in the range between 0,013 $mm.s^{-1}$ to 0,021 $mm.s^{-1}$ which was fulfilled during our testing. Self-aligning devices for applying the tensile load to the assembly of the coating and fixtures did not permit eccentric load or bending moment to the specimen. All specimens were degreased in acetone prior to testing.

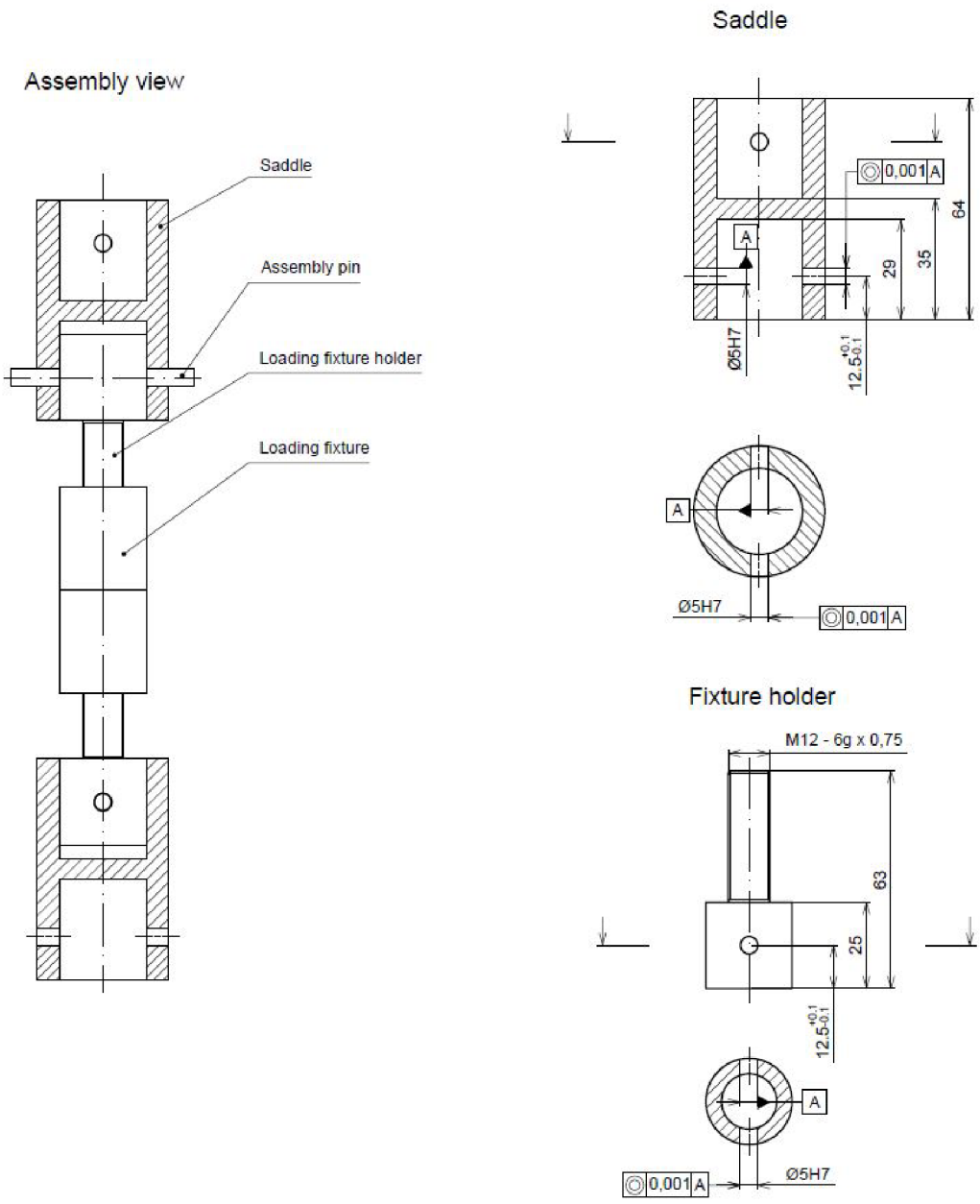


**Figure 29 - Setup used for adhesion testing**

## 3.3.2. Fixing Tool

The adhesive bonding agent used for testing was FM1000 made by Cytec company (USA). It requires curing for 1 hour at 442 K under activation load of 140 N. To achieve the pre loading strength, a fixing device was developed within the scope of this thesis. Its construction can be seen in Figure 30. All parts were cut on laser CNC machine which achieves cutting to the precision of 0,1 mm. The holes in the fixating plate have diameter 25,0 mm to accommodate the substrates. The frame of the device was bent on a bending machine. After adding the samples and assembling, springs are put on top of each substrate/fixture stack and then another plate is put on top of that assembly. Thereby, the load is applied (1120 N for the whole assembly) and the loading plate is fixed in the required position by two stoppers. The springs used were manufactured by Alcomex Spring Works s.r.o. and the dimension are 2,5 x 20,0 x 36,0 mm.

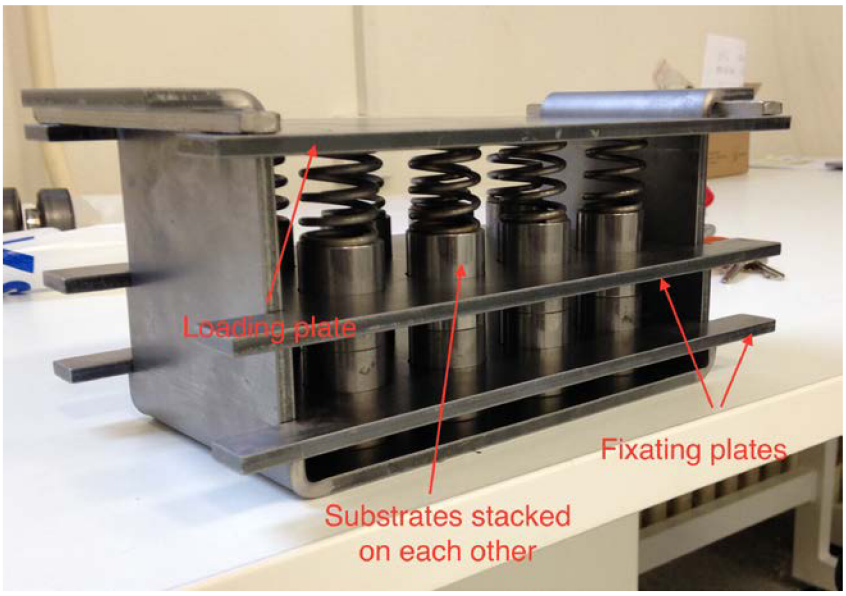


**Figure 30 – Pre-loading device with substrates stacked inside and load applied**

It was decided that total 5 series of tests are going to be carried out to test the tensile bonding strength of the adhesive film, coating tensile strength in as-sprayed modified condition.

## 3.4. Metallographic and Chemical Analysis

Metallographic analysis was carried out using light microscope Axio Vert A1 and electron microscope FEG SEM Zeiss Ultra Plus both made by the Zeiss company. Light microscope metallographic analysis served for evaluation of microstructure after EB each optimization step. SEM metallographic analysis was used to analyze the reference samples from each of the final modified series.

All specimens used for metallographic and chemical analysis were mounted using Leco PR-4X. The prepared metallurgical mount was then subjected to series of grinding on a Struers Pedemin-2 device using silicon carbide abrasive papers. Each specimen was grinded on 5 abrasive papers with the grit size range 220, 320, 500, 800 and 1000 (4 minutes of specimen grinding on each abrasive paper). The specimen were polished to remove the abrasion-damage layer that includes plastically deformed material and the slip/twin/shear damage immediately beneath the surface. Polishing was again carried out on Struers Pedemin-2**.** 3 µm and 1 µm diamond polish were used and polishing times were 4 minutes for each grade.

Electron microcopy was used to analyze coating/substrate interface for the two chosen EB modifications. Depth of the modified zone was measured and EDX module was used to perform chemical analysis. It is important to note that during the chemical analysis, the values of carbon were not taken into account. The analysis was carried out for the modified layer and for analysis of the dark phases formed on the surface of the substrates after EB modification.

## 3.5. Evaluation of Microhardness

Vickers microhardness measurements were carried out following guidelines provided by CSN EN ISO 6507 standard. The indenter used in these measurements is a diamond pyramid with the apex angle of 136° (Figure 31). Tests were carried out on a LECO microhardness tester LM 247AT.

When measuring the microhardness, loading force of 1 N had been applied. The specimen were prepared properly in the form of metallographic sample. The time since the beginning of applying maximum load was be in the range of 2 to 8 s while the rate of loading did not exceed 0,2 $mm.s^{-1}$. Vickers hardness the calculated by the following equation:

$$HV = \frac{2F sin\frac{136°}{2}}{d^2} \tag{1}$$

Where *F* is a load in kg, *d* is an arithmetic mean of the two diagonals, *d1* and *d2* in mm and HV stands for Vickers hardness.

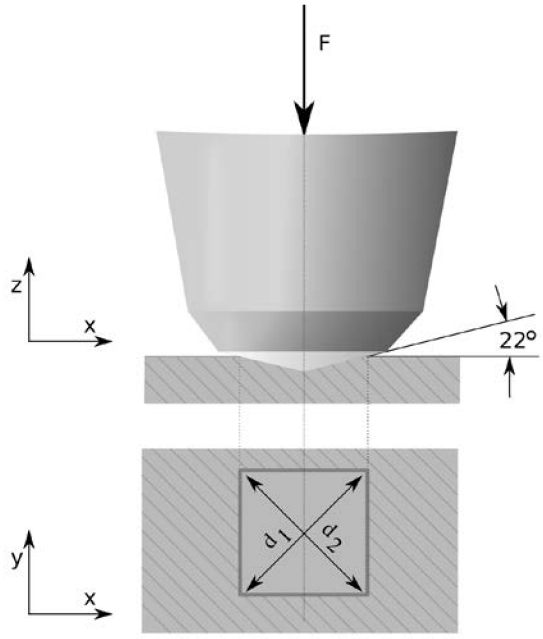


**Figure 31 - Scheme of Vickers hardness apparatus setup**

# 4. Results and Discussion

## 4.1. Microstructure Analysis

In this section will be discussed the microstructure and the coating/substrate interface of the coating in as-sprayed condition as well as the modified layer. Metallographic analysis was carried out using electron and light microscope and stereo magnifier as described in chapter 3.4.

The microstructure of the coating from series A in as-sprayed condition can be seen in the Figure 32. In the as-prayed coating structure individual splats are apparent, which is typical for plasma sprayed coatings. Oxides are present which was confirmed by the EDX analysis (see Chapter 4.3), as well as porosity. Roughness appears to be relatevily high. It also appears that little to none metallurgical bonding occurred with the substrate and the primary adhesion mechanism of the coating is expected to be mechanical anchorage. In the case of series B and C the porosity decreased as well as roughness. Quality of the substrate/coating interface was clearly different. No pores were present at the interface and the microstructure suggested that mixing of the substrate and the coating material occurred (Figure 33).

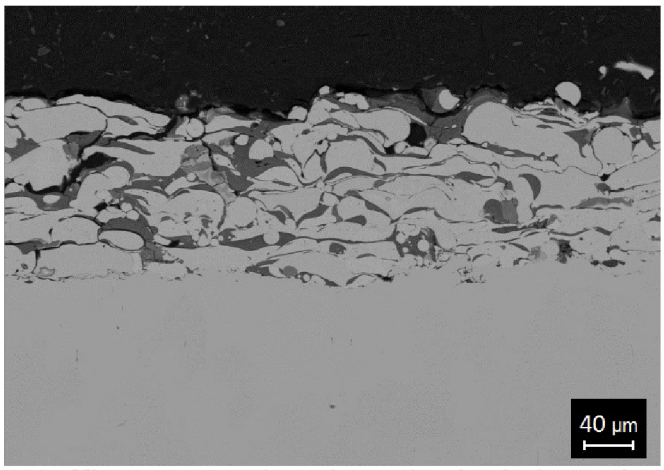


**Figure 32 - Microstructure of specimen of series A observed on SEM**

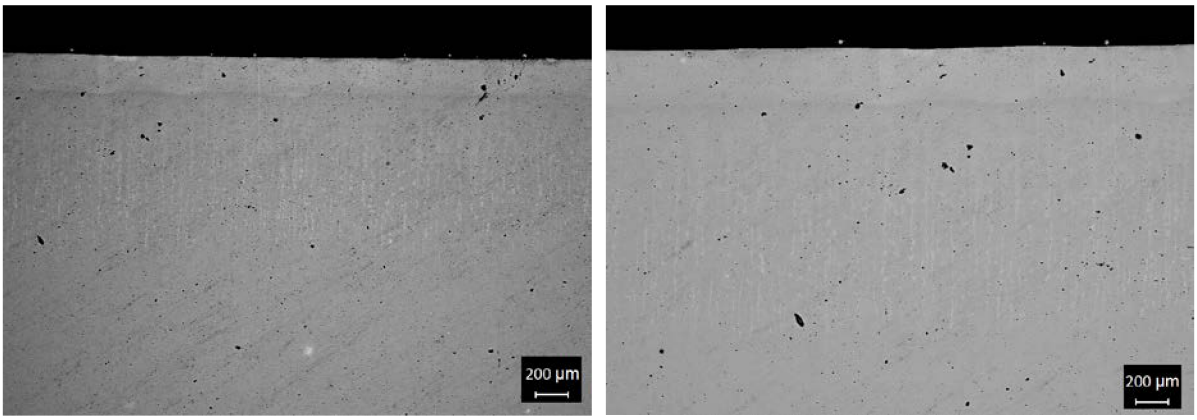


**Figure 33 - Microstructures of the modified layers: Left - Series B, Right - Series C**

The specimens from both B and C series (Figure 34) had a dark layer on the surface that formed after the modification. It composed of a phase different from the rest of the modified coating layer. Spallation of this phase occurred during cooling after the electron beam deposition, suggesting it is a brittle phase with different thermal expansion coefficient than the rest of the modified coating. Results from EDX analysis identified these phases as $Al_2O_3$ and $Y_2O_3$ (see chapter 4.3). The oxides formed on the surface correlated with the oxide content in the microstructure of the coating. Given that the EB modification was performed in a vacuum (no significant oxidation during modification is expected) and that the coating/substrate material were in a molten state during the modification it was concluded that the oxides from the original microstructure floated up to the surface (ratio of the densities is approximately 1:4, oxides being the less dense phase). The oxide phase exhibits a dendritic structure (Figure 35). Because oxides from the original coating do not exhibit this kind of structure, it can be concluded that these phases melted and resolidified on the surface during the EB modification.

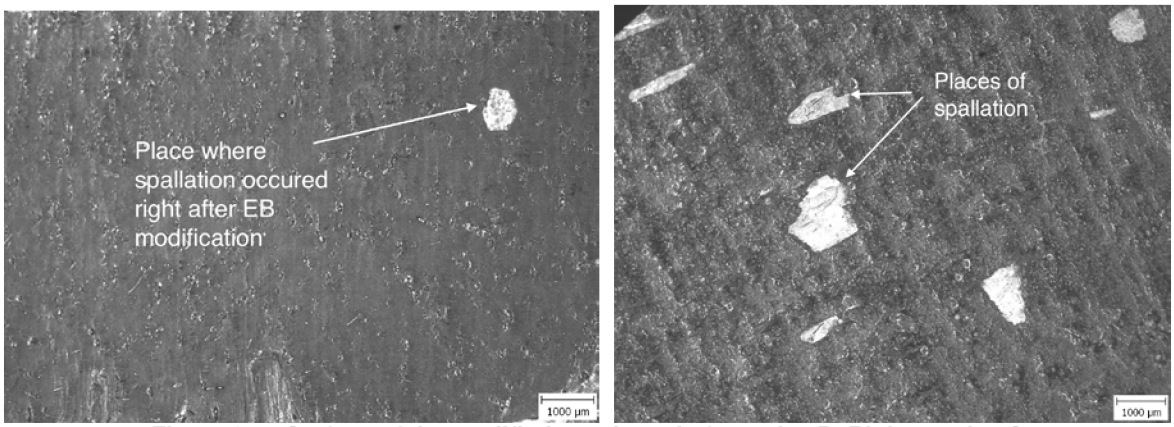


**Figure 34 – Surface of the modified specimen Left - series B. Right - series C**

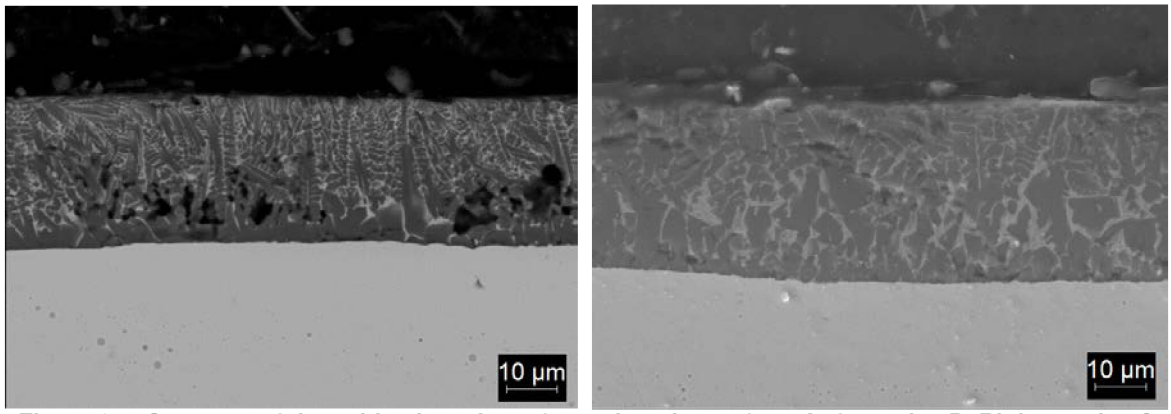


**Figure 35 - Structure of the oxide phase layer formed on the surface: Left - series B, Right - series C**

## 4.2. Coating and Modified Layer Thickness Analysis

The thickness of coating in as-sprayed condition and modified layers was analyzed using light microscopy using a dedicated software. The results of the measurements can be seen in the Table 5. It should be noted that in case of series B and C the oxide layer is included in the thickness. Also it should be taken into account that during the EB modification spark emission occurred and some of the coating material has been dispersed around the vacuum chamber.

**Table 5 - Results of the layer thickness measurements of series A, B and C (in µm)**

| Series A | Series B | Series C |
|---|---|---|
| Ø 149,3 ± 24,0 | Ø 170,3 ± 26,7 | Ø 184,5 ± 13,8 |

From the results it can be seen that series C had higher thickness of the modified layer. This was most likely caused by different EB parameters which resulted in higher heat energy input into the material.

## 4.3. Chemical Analysis

Chemical composition of coatings and substrates was studied using EDX module of an electron microscope. Both EDX mapping and linear analysis was used. Changes in chemical composition occurred after the EB modification, mainly due to the material mixing of the substrate/coating material.

Chemical composition of the series A using EDX mapping can be seen in the Table 6. The analysis showed that oxides were present. From in-flight particle temperature that was discussed in the Chapter 3.1.5 it can be concluded that oxides originated from the inflight particle oxidation during WSP spraying. For series B and C linear EDX analysis was carried out to see whether or not mixing of substrate and coating occurred. Because similar results were obtained from both series (except that the depth of material mixing is about 30 µm larger, most likely due to larger energy input) only results from linear EDX analysis of series B will be commented (results from series C can be seen in the Figure 37). In the results from the linear EDX analysis of series B there are three distinguishable regions (Figure 36). One in the range of 0 µm (0 µm representing the surface of the specimen) to about 30 µm which belongs to the composition of oxide phase formed on the surface. From the EDX measurement it could be seen that this layer is high in aluminum yttrium and oxygen content, aluminum being the dominant phase. Next region is in the range of 30 to 200 µm where mixing of the substrate and the coating material occurred and the third region starts at 200 µm where the chemical composition corresponds to that of the substrate (for series C the ranges are: 400-350 µm for oxide layer; 350-170 µm material mixing; 170-0 µm substrate material). Using the EDX mapping it was concluded that the layer composed mainly from $Al_2O_3$ and $Y_2O_3$.

**Table 6 - Results EDX mapping of series A layer (in wt. %)**

| Ni | Cr | Al | O | Y |
|---|---|---|---|---|
| 57,2 | 17,6 | 15,3 | 8,0 | 0,7 |

Mixing of the substrate and the coating layer material is most obvious from the evolution of the wt.% curves of Fe and Ni from the EDX linear analysis in the 30-200 µm region, as no Fe was present prior the modification in the coating layer and no Ni was present in the substrate. The wt.% of Fe is about 5 wt.% right below the oxide layer and gradually increases with the increasing depth with direction into the substrate. At about 150 um the concentration gets on par with Ni content (40 wt.%.). This supports the

assumption that was made during the metallographic analysis that good material mixing occurred at the substrate/coating interface and that metallurgical bonding most likely occurred.

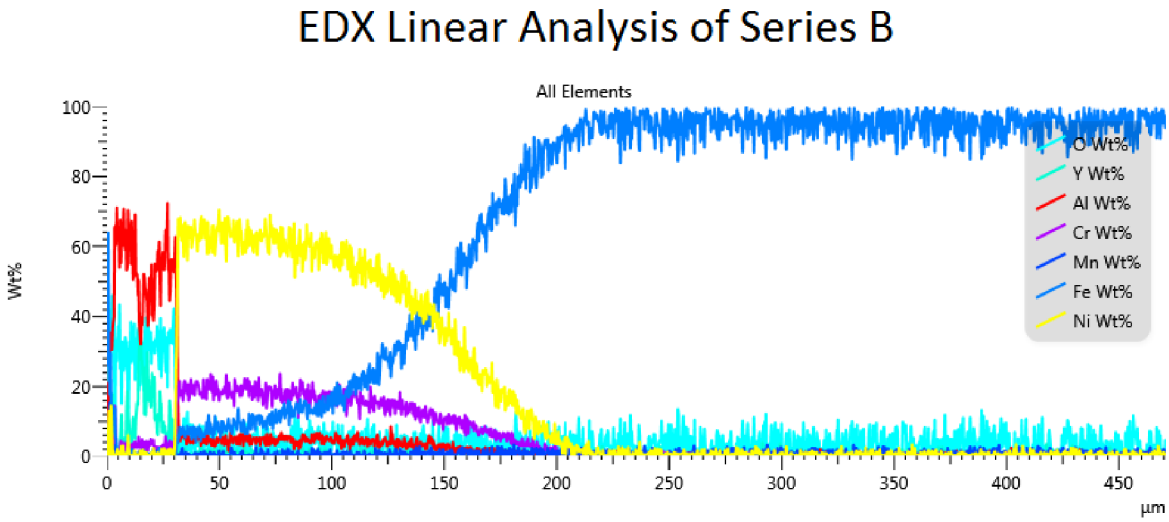


**Figure 36 - Linear EDX analysis of the series C**

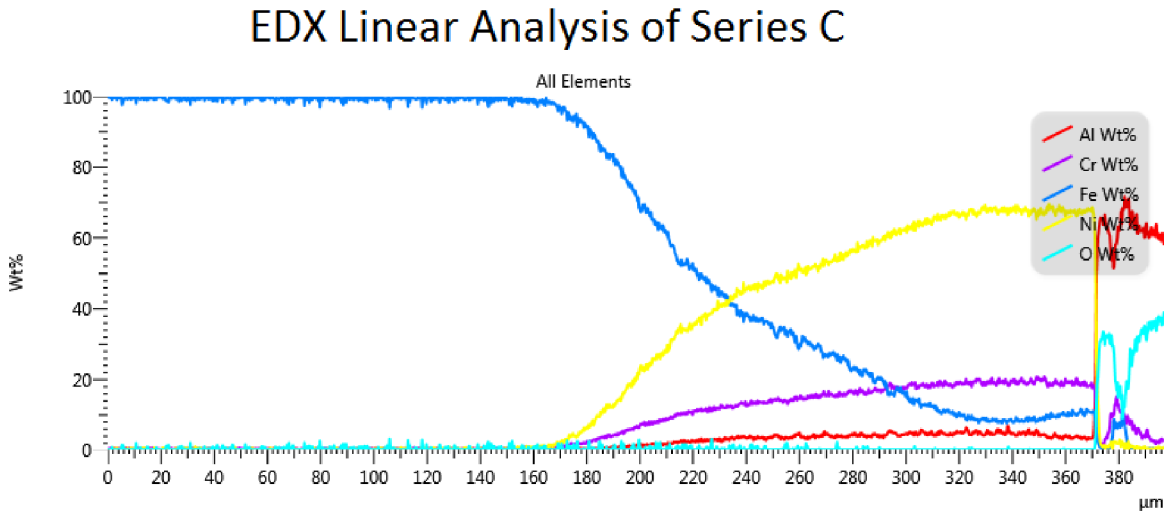


**Figure 37 – Linear EDX analysis of the series C**

The wt.% of Al in the modified layer below the surface oxide is fairly low and drops below 5 %, while in the original coating it was found to be 15,4 %, so the depletion of Al in the layer could be explained by formation of $Al_2O_3$ on the surface. Because little to no oxidation was expected to occur during the EB modification the low content suggests that most of the Al oxidized during the deposition. This is also evident from high Al content in the surface oxide layer in results from EDX linear analysis

XRD analysis was carried out on samples from series A, B and C and summarized data can be seen in the Table 7. It was found that the series A with coating in as-sprayed condition several phases were present, the most dominant being Ni – (Cr) and NiAl which is a typical structure for MCrAlY type of coatings. $Ni_5Y$ phase is an intermetallic phase and is known to form in plasma spray coatings due to low solubility of Y in Ni solid solution

[41]. Oxide phases present in the series A microstructure are most likely a results of in-flight oxidation during deposition.

After electron beam modification only one phase was present and that was a solid solution of Ni as can be seen in the Figure 39. Because the results of XRD analysis of series B and C were almost the same (only difference is that there was impurity $NiCO_3$ present in small quantity in the series C; results in Figure 40), for this reason only results from analyzing series B are commented. No NiAl or $Ni_3Al$ phases were present. There might be several reasons for this. First one might be the presence of Fe in fairly high content (about 10 wt.% at the surface), which stabilized the Ni solution and only one phase was formed. The second one may be a fairly low content of Al which was according to EDX linear analysis below 5 wt. % together with chemical composition homogenization that most likely occurred during EB modification. Therefore the Al may have dissolved in the Ni solid solution as all other elements.

**Table 7 - Summarized results from the XDR analysis of A, B and C series (in wt. %)**

| | Powder | Series A | Series B | Series C |
|---|---|---|---|---|
| Ni solid solution | 67,3 | 76,2 | 100 | 98,4 |
| NiAl | 32,7 | 12,3 | 0 | 0 |
| $Ni_5Y$ | 0 | 2,9 | 0 | 0 |
| NiO | 0 | 1,7 | 0 | 0 |
| $NiAl_2O_4$ | 0 | 7 | 0 | 0 |
| $NiCO_3$ | 0 | 0 | 0 | 1,6 |

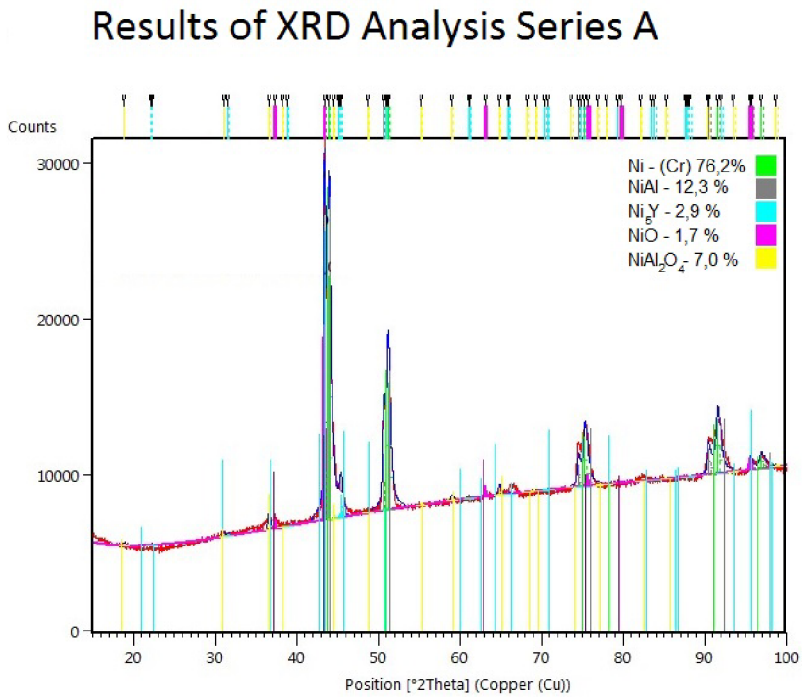


**Figure 38 - Results of XRD analysis of specimen from series A**

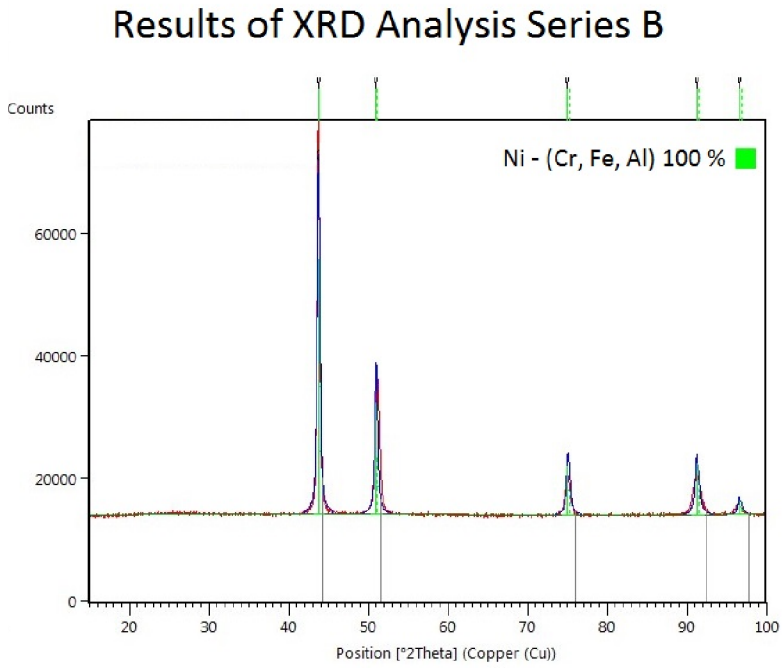


**Figure 39 – Results of XRD analysis of specimen from series B**

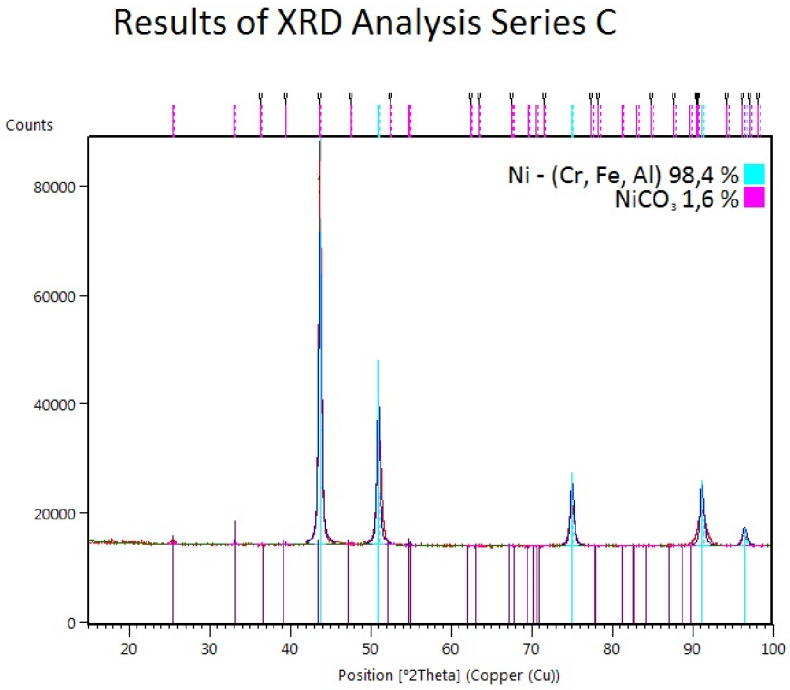


**Figure 40 – Results of XRD analysis of series C**

## 4.4. Evaluation of Microhardness

The method used for microhardness measurement was described in the chapter 3.6.

Microhardness of the A series with coating in as-sprayed condition varied widely. This was due to oxide content in the layer. Oxides had higher microhardness than the splats therefore the results of measurements of microhardness of series A coating has a high variance. Microhardness of the B and C series with coatings modified by the EB was considerably lower than in the cause of series A. This was expected as the EB modification caused all the oxides in the original coating structure to move up to the surface and the diffusion of Fe into the layer after the modification could also be the reason for the decrease. The results can be seen in the Table 8.

**Table 8 - Results of microhardness measurements (in HV 0,1)**

| Series A | Series B | Series C | Substrate |
|---|---|---|---|
| Ø 276 ± 68 | Ø 199 ± 15 | Ø 188 ± 9 | Ø 194 ± 14 |

Evolution of microhardnes in the direction into the substrate was also analyzed to reveal the effect of EB modification on the substrate microhardness. The results can be seen in the Figure 41. There are three distinguishable regions: Area I in the range of 0 to 0,2 mm (0 representing the surface), which represents the area of the original coating. Then Area II in the range of 0,2 to 0,5 mm where hardening for specimens from series B and C occurred and Area III where the hardness of the base material returns to normal for all series. Hardenability of low carbon steels is generally poor, however some hardening occurred in the case of B and C series. Larger hardening occurred for series B. The reason hardening in the case of series C was not as high could that the energy input during the EB modification was about 50% higher, therefore it is expected that after hardening tempering of the modified layer occurred to a larger degree in the case of series C and caused lowering of the hardness.

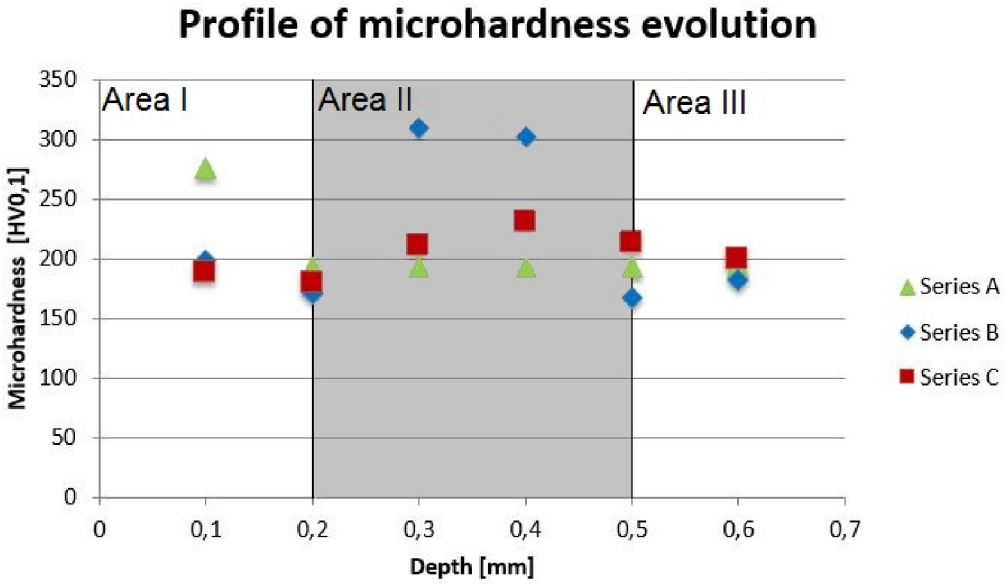


**Figure 41 - Hardness evolution in the direction into the substrate**

## 4.5. Adhesion testing

Adhesion tests were carried out using an experimental setup and method described in Chapter 3.3.

Total 5 series of tests were carried out plus 2 series of tests to find out the influence of acetone degreasing on the bonding strength of FM1000. The results can be seen in the Table 8. First series tested had no coating applied and served only as a way to determine adhesive strength of the FM1000. The adhesive strength is higher than estimated adhesive strength of coatings sprayed with WSP technology. Bonding agent is therefore suitable for adhesive strength testing of these coatings.

**Table 9 - Summarized data from adhesion strength testing**

| Series | Tensile adhesive strength [MPa] | Number of tested samples |
|---|---|---|
| FM1000 only - Grinded fixtures | Ø 69,4 ± 2,2 | 8 |
| Series A - Sandblasted fixtures | Ø 22,8 ± 1,4 | 8 |
| Series B (with oxide layer) - Sandblasted fixtures | Ø 13,9 ± 5,0 | 8 |
| Series B (grinded) - Sandblasted fixtures | Ø 22,1 ± 7,6 | 8 |
| Series C (grinded) - Grinded fixtures | Ø 32,0 ± 3,3 | 8 |
| FM1000 only - Grinded fixtures (degreased) | Ø 46,0 ± 0,6 | 2 |
| FM1000 only - Grinded fixtures (no degreasing) | Ø 47,2 ± 0,8 | 2 |

In next series of tests specimens from series A with coatings in as-sprayed condition were tested. Results can be seen in the Table 9. From the analysis of the fractured surface it could be seen that cohesive failure occurred (Figure 42). Low cohesive strength of the coating was most likely caused by not optimized deposition parameters, leading to high oxide content, discontinuities and porosity and also by individual splat structure.

**Figure 42 - Series A after adhesion testing**

On the modified B specimens two series of tests were carried out. The first one was to determine the adhesive strength of the oxide layer that formed on the surface. The adhesive strength was however quite low and varied significantly as can be seen from the variance of the results in Table 9. In another series of tests the B specimens were in

grinded condition to remove the oxide layer formed during EB modification. The measured adhesive strength in this case does not correspond to real value of the B series coating adhesion as the failure occurred at the glue-coating interface, adhesive strength of the modified layer of series B is therefore greater than the value measured. Results can be seen in the Table 9. This could have been a consequence of improper bonding (Figure 43) of the FM1000 agent to the surface. Further testing is planned to overcome this problem and obtain the modified coating adhesive strength.

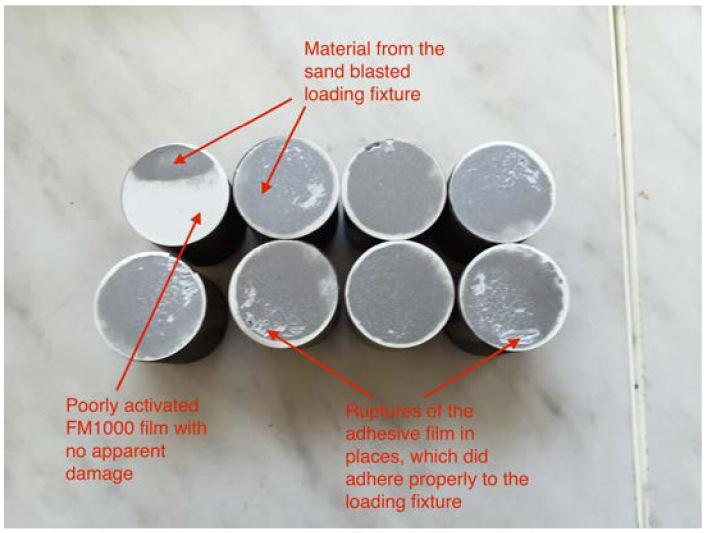


**Figure 43 - Series of adhesion tests of specimen B (grinded). Failure occurred in the adhesive film**

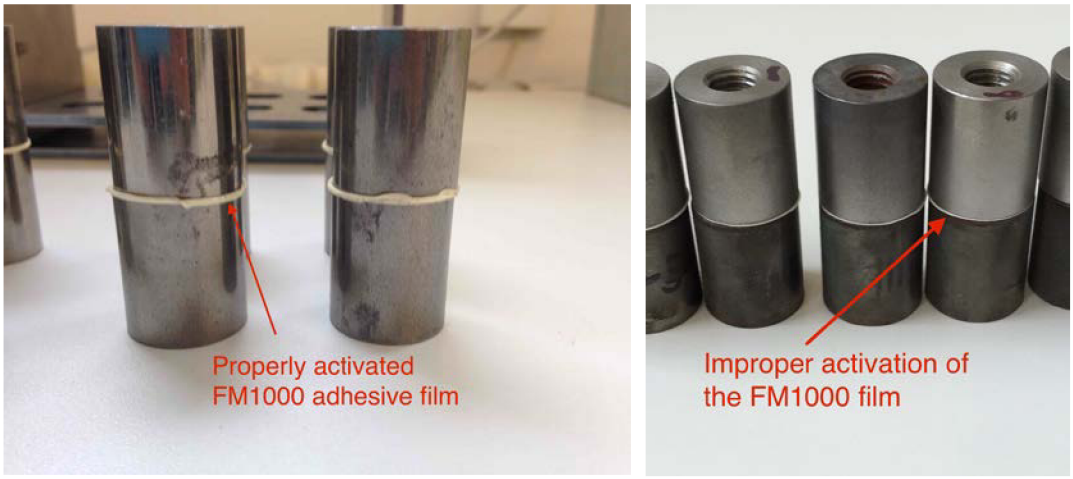


**Figure 44 - Left - FM1000 activation before the first FM1000 series of tests. Right - FM1000 activation before the B series of tests (oxide layer)**

The problem seemed to be in the activation of the adhesive film (see Figure 44). It looked like the adhesive had a too high surface tension to get into proper contact with the sandblasted surface of the loading fixture. That also suggest the remnants of the blasted loading fixture material on the adhesive film (Figure 43). The adhesive film got into proper contact only with the higher parts of blasted rough profile and these were ripped out during the adhesion testing. Because all the specimen were degreased in acetone, we further investigated its effect on the bonding strength. Because blasting seemed to be causing problems, the loading fixtures used for testing the influence of acetone on bonding strength were grinded on a magnetic grinder to achieve a smooth surface.

It was found that acetone degreasing had little to no effect on the bonding strength of the FM1000 and the results can be seen in Table 9 (subsequent FM1000 tests), however the bonding strength decreased by 33 % as opposed to the FM1000 only for unidentified reason, improper bonding agent activation occurred in both cases.

Because grinded fixtures exhibited better adhesive strength than sandblasted fixtures adhesion tests on series C were carried out using grinded loading fixtures. Improper activation occurred again and the measured adhesive strength again does not correspond to real value of the C series coating adhesion as the failure occurred at the glue-coating interface (see Figure 45), adhesive strength of the modified layer of the series C is therefore greater than the value measured. Results can be seen in the Table 8. However this time the adhesive strength measured was significantly higher than that of that of the series A (by approximately 40%). Therefore it can be concluded that the EB modification in the case of series C did significantly increase the coating adhesive strength of the WSP sprayed NiCrAlY coating.

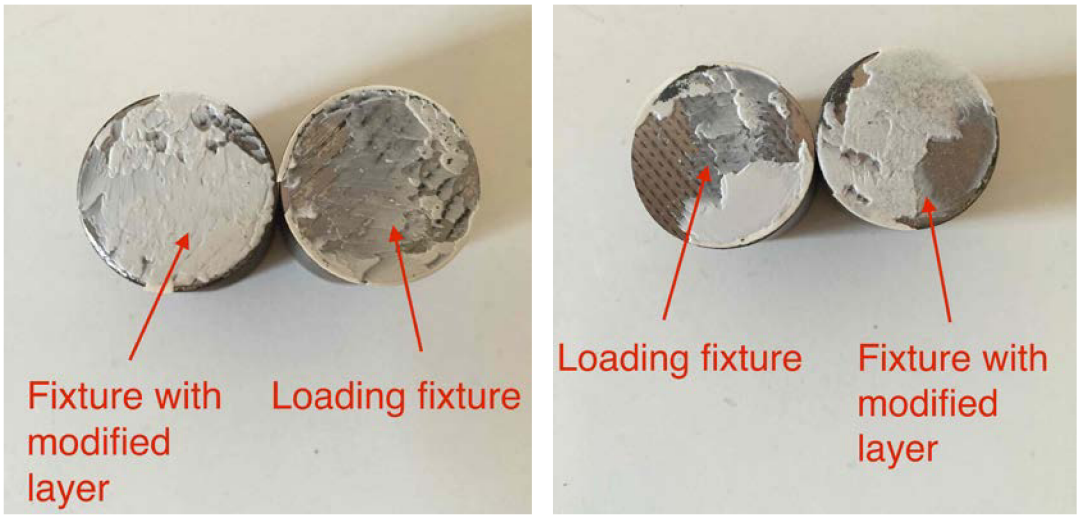


**Figure 45 - Specimen from series C after adhesion testing**

# 5. Conclusions

The objectives of this thesis were to study modifications of the substrate/coating interface of thermally sprayed NiCrAlY bond-coatings with the electron beam technology and to attempt to determine the influence of the EB modification on the quantitative values of tensile adhesive strength of the modified layers.

- The NiCrAlY coatings were successfully deposited using WSP technology. WSP is therefore suitable technology for deposition of NiCrAlY coatings. The coating chemical composition was different to that of the feedstock powder. The difference was caused mainly by oxidation of the NiCrAlY material during the deposition.

- EB modification of the coating-substrate interface was successfully carried out and mixing of the substrate and coating material occurred. EB technology is therefore suitable for remelting of NiCrAlY coatings. The EB modification of the NiCrAlY coatings led to increase in quality of the substrate-coating interface and metallurgical bonding most likely occurred.

- Phase composition of the EB modified layers changed when compared to that of the coating in the as-sprayed condition. This was caused by homogenization of the coating layer chemical composition, displacement of the oxides to the surface, and diffusion of Fe from the substrate.

- The EB modification of the NiCrAlY layer caused fusing of the $Al_2O_3$, $Y_2O_3$ oxides within the original coating microstructure and dislocating them onto the surface forming a homogenous oxide layer. Due to dendritic structure of the oxide layer it was concluded that the oxides from the original coating structure were heated up enough to reach the liquid phase. Reason why these phases were dislocated onto the surface could be the difference in density of the oxides and rest of the material.

- Coatings in as sprayed condition failed cohesively during the adhesion tests. This was caused most likely by oxide content, porosity and intersplat voids. Adhesion tests of the modified layers of series B and C failed prematurely at the coating-adhesive interface due to unidentified reason and will be investigated in study follow-up. Because EB modification of series B and C removed possible sources of the cohesive failure that occurred in series A, it is expected that cohesive strength of the modified layers is higher. This assumption was neither denied or proven when testing series B due to already mentioned premature failure at the substrate-bonding agent interface during testing, however it was proven correct when testing series C where the results showed the cohesive strength is at least 40 % higher than that of the layer in as-sprayed condition in series A.

- For the adhesion testing of EB modified layers study follow-up, it is recommended to deposit a layer of higher thickness (exceeding 400 μm) so that the surface can be finished to remove the formed oxide scale and to achieve planar surface geometry.

# 6. Refferences


[1] Tucker: ASM Handbook 5A: Thermal Spray Technology, ASM International, 2013

[2] *Cold spray technology*. 1st ed. Amsterdam: Elsevier, 2007, xii, 328 s., [2] s. bar. příl. ISBN 978-0-08-045155-8.

[3] *Thermal spray 2004: advances in technology and application : proceedings of the International Thermal Spray Conference, 10-12 May, 2004, Osaka, Japan*. 2004. Materials Park, Ohio: ASM International, xxix, 1118 p. ISBN 08-717-0809-4.

[4] FRIDMAN ., ed. by A.. 2007. *Transport phenomena in plasma*. 1. ed. Amsterdam [u.a.]: Elsevier. ISBN 978-012-3739-230.

[5] FAUCHAIS, P, Eiji NISHIOKA, Takeshi NISHIYAMA, D.R. NAGY a P.C. PATNAIK. Understanding plasma spraying. Journal of Physics D: Applied Physics. 2004, 37(9): R86-R108. DOI: 10.1088/0022-3727/37/9/R02. ISSN 0022-3727. Availible at: http://stacks.iop.org/0022-3727/37/i=9/a=R02?key=crossref.538c8a1caa8ac149ec9c47a9939f138d

[6] BOULOS, M. I. RF induction plasma spraying: State-of-the-art review. Journal of Thermal Spray Technology. 1992, 1(1): 33-40. DOI: 10.1007/BF02657015. ISSN 1059-9630. Availible at: http://link.springer.com/10.1007/BF02657015

[7] MORAVEC, J., M. HRABOVSKY a R. MATAS. 2002. *DESIGN AND MODIFICATION OF WATER- STABILIZED PLASMA GENERATOR*.

[8] XIONG, Hong-Bing, Li-Li ZHENG, Li LI a Anirudha VAIDYA. Melting and oxidation behavior of in-flight particles in plasma spray process. International Journal of Heat and Mass Transfer. 2005, 48(25-26): 5121-5133. DOI: 10.1016/j.ijheatmasstransfer.2005.07.019. ISSN 00179310. Availible at: http://linkinghub.elsevier.com/retrieve/pii/S0017931005004771

[9] FUKUMOTO, Masahiro, Eiji NISHIOKA, Takeshi NISHIYAMA, D.R. NAGY and P.C. PATNAIK. New criterion for splashing in flattening of thermal sprayed particles onto flat substrate surface. Surface and Coatings Technology. 2002, 161(2-3): 103-110. DOI: 10.1016/S0257-8972(02)00471-1. ISSN 02578972. Availible at: http://linkinghub.elsevier.com/retrieve/pii/S0257897202004711

[10] KAMEDA, J., T.E. BLOOMER a S. SAKURAI. Oxidation/Carbonization/Nitridation and In-Service Mechanical Property Degradation of CoCrAlY Coatings in Land-Based Gas Turbine Blades. Journal of Thermal Spray Technology. 8(3): 440-446. DOI: 10.1361/105996399770350403. ISSN 00000000. Availible at: http://link.springer.com/10.1361/105996399770350403

[11] VARDELLE, A., M. VARDELLE, H. ZHANG, N. J. THEMELIS a K. GROSS. Volatilization of Metal Powders in Plasma Sprays. Journal of Thermal Spray Technology. 2004, 11(2): 244-252. DOI: 10.1361/105996302770348907. ISSN 00000000. Availible at: http://link.springer.com/10.1361/105996302770348907

[12] WEISS, H., M. VARDELLE, H. ZHANG, N. J. THEMELIS a K. GROSS. Adhesion of advanced overlay coatings: mechanisms and quantitative assessment. Surface and Coatings Technology. 1995, 71(2): 201-207. DOI: 10.1016/0257-8972(94)01022-B. ISSN 02578972. Availible at: http://linkinghub.elsevier.com/retrieve/pii/025789729401022B

[13] ZAAT, J H. 1983. A Quarter of a Century of Plasma Spraying. *Annual Review of Materials Science*. **13**(1): 9-42. DOI: 10.3403/30133129.

[14] FAUCHAIS, P., M. VARDELLE, A. VARDELLE, L. BIANCHI a K. GROSS. Plasma spray: Study of the coating generation. Ceramics International. 1996, 22(4): 295-303. DOI: 10.1016/0272-8842(95)00106-9. ISSN 02728842. Availible at: http://linkinghub.elsevier.com/retrieve/pii/0272884295001069

[15] PAREDES, R.S.C., S.C. AMICO, A.S.C.M. D'OLIVEIRA, L. BIANCHI a K. GROSS. The effect of roughness and pre-heating of the substrate on the morphology of aluminium coatings deposited by thermal spraying: Study of the coating generation. Surface and Coatings Technology. 2006, 200(9): 3049-3055. DOI: 10.1016/j.surfcoat.2005.02.200. ISSN 02578972. Availible at: http://linkinghub.elsevier.com/retrieve/pii/S0257897205004408

[16] MELLALI, M., P. FAUCHAIS a A. GRIMAUD. Influence of substrate roughness and temperature on the adhesion/cohesion of alumina coatings. 1996, 81(2-3): 275-286. DOI: 10.1016/0257-8972(95)02540-5. ISSN 02578972. Availible at: http://linkinghub.elsevier.com/retrieve/pii/0257897295025405

[17] LEE, C.H., H.K. KIM, H.S. CHOI a AHN. Phase transformation and bond coat oxidation behavior of plasma-sprayed zirconia thermal barrier coating. Surface and Coatings Technology. 2000, 124(1): 1-12. DOI: 10.1016/S0257-8972(99)00517-4. ISSN 02578972. Availible at: http://linkinghub.elsevier.com/retrieve/pii/S0257897299005174

[18] CONTRERAS, M.E., H. OROZCO and A. MEDINA-FLORES*. 2008. *Structural analysis of ytria partially stabilized zirconia*. [cit. 2015-05-11].

[19] YUAN, Kang, Ru LIN PENG, Xin-Hai LI, Sten JOHANSSON a Yan-Dong WANG. Some aspects of elemental behaviour in HVOF MCrAlY coatings in high-temperature oxidation. Surface and Coatings Technology. 2015, 261(1): 86-101. DOI: 10.1016/j.surfcoat.2014.11.053. ISSN 02578972. Availible at: http://linkinghub.elsevier.com/retrieve/pii/S0257897214010743

[20] MOON, Jaeyun, Hanshin CHOI, Hyungjun KIM, Changhee LEE a F.S. PETTIT. The effects of heat treatment on the phase transformation behavior of plasma-sprayed stabilized ZrO2 coatings. Surface and Coatings Technology. 2002, 155(1): 1-10. DOI: 10.1016/S0257-8972(01)01661-9. ISSN 02578972. Available at: http://linkinghub.elsevier.com/retrieve/pii/S0257897201016619

[21] BUTZ, Benjamin. 2009. *Yttria-Doped Zirconia as Solid Electrolyte for Fuel-Cell Applications*. Otterdstadt. Dissertation thesis. Fakult¨at fu¨r Physik des Karlsruher Institutes fu¨r Technologie.

[22] SHEU, Tzer-Shin, Tseng-Ying TIEN, I-Wei CHEN, G.H. MEIER a F.S. PETTIT. Cubic-to-Tetragonal (t') Transformation in Zirconia-Containing Systems. Journal of the American Ceramic Society. 1992, 75(5): 1108-1116. DOI: 10.1111/j.1151-2916.1992.tb05546.x. ISSN 0002-7820. Available at : http://doi.wiley.com/10.1111/j.1151-2916.1992.tb05546.x

[23] EVANS, A.G., D.R. MUMM, J.W. HUTCHINSON, G.H. MEIER a F.S. PETTIT. Mechanisms controlling the durability of thermal barrier coatings. Progress in Materials Science. 2001, 46(5): 505-553. DOI: 10.1016/S0079-6425(00)00020-7. ISSN 00796425. Available at: http://linkinghub.elsevier.com/retrieve/pii/S0079642500000207

[24] BOSE, Sudhangshu. 2007. *High temperature coatings*. 30 Corporate Drive, Suite 400, Burlington, MA 01803, USA: Elsevier In.c. ISBN 978-0-7506-8252-7.

[25] ACHAR, D.R.G., R. MUNOZ-ARROYO, L. SINGHEISER, W.J. QUADAKKERS a Yan-Dong WANG. Modelling of phase equilibria in MCrAlY coating systems. Surface and Coatings Technology. 2004, 187(2-3): 272-283. DOI:

10.1016/j.surfcoat.2004.02.018. ISSN 02578972. Availible at: http://linkinghub.elsevier.com/retrieve/pii/S0257897204001495
[26] CHEN, W.R., X. WU, B.R. MARPLE, P.C. PATNAIK a Yan-Dong WANG. Oxidation and crack nucleation/growth in an air-plasma-sprayed thermal barrier coating with NiCrAlY bond coat. Surface and Coatings Technology. 2005, 197(1): 109-115. DOI: 10.1016/j.surfcoat.2004.06.027. ISSN 02578972. Availible at: http://linkinghub.elsevier.com/retrieve/pii/S0257897204004785
[27] DRAGOS, Utu, Marginean GABRIELA, Brandl WALTRAUT, Cartis IOAN a F.S. PETTIT. Improvement of the oxidation behaviour of electron beam remelted MCrAlY coatings. Solid State Sciences. 2005, 7(4): 459-464. DOI: 10.1016/j.solidstatesciences.2005.01.003. ISSN 12932558. Available at: http://linkinghub.elsevier.com/retrieve/pii/S1293255805000154
[28] CHEN, W.R., X. WU, B.R. MARPLE, D.R. NAGY a P.C. PATNAIK. TGO growth behaviour in TBCs with APS and HVOF bond coats. Surface and Coatings Technology. 2008, 202(12): 2677-2683. DOI: 10.1016/j.surfcoat.2007.09.042. ISSN 02578972. Available at: http://linkinghub.elsevier.com/retrieve/pii/S0257897207010134
[29] PACE, M. T., R. C. THOMSON, B.R. MARPLE, D.R. NAGY a P.C. PATNAIK. Oxidation of MCrAlY coatings on Ni based superalloys. Energy Materials. 2007, 2(3): 181-190. DOI: 10.1179/174892408X373545. ISSN 1748-9237. Available at: http://www.maneyonline.com/doi/abs/10.1179/174892408X373545
[30] BAUER, Branko a Matija BUSIC. Recently the technology of high power density heat sources such as electron and laser beams has gone through a rapid development and is being applied in welding, cutting [online]. [cit. 2015-05-21]. Available at: http://www.eolss.net/sample-chapters/c05/e6-171-06-00.pdf
[31] ASM handbook. 6th print. Materials Park: ASM International, 2003. ISBN 08-717-0382-3.
[32] AMERICAN WELDING SOCIETY (AWS) C7 COMMITTEE ON HIGH ENERGY BEAM WELDING AND CUTTING. Recommended practices for electron beam welding and allied processes. 4th edition. 2013. ISBN 978-087-1718-358.
[33] SMALLMAN, R. Modern physical metallurgy and materials engineering: science, process, aplications. 6th ed. Oxford: Butterworth-Heinemann, 1999, 438 s. ISBN 07-506-4564-4.
[34] KRAUSS, George. Steels: processing, structure, and performance. Materials Park, Ohio: ASM International, 2005, xix, 613 p. ISBN 08-717-0817-5.
[35] Ionbond [online]. [cit. 2015-05-21]. Available at: http://www.ionbond.cz/
[36] KOREA AEROSPACE UNIVERSITY. Electron Beam Welding [online]. 2009 [cit. 2015-05-21]. Available at: http://mercury.kau.ac.kr/welding/Welding%20Technology%20I%20-%20Welding%20Processes/Chapter%209%20-%20Electron%
[37] ZENKER, R. MODERN THERMAL ELECTRON BEAM PROCESSES – RESEARCH RESULTS AND INDUSTRIAL APPLICATION. 2009. Available at: http://www.gruppofrattura.it/pdf/ext/AIM/Anno%202009/Marzo/New%20electron%20beam%20liquid-phase%20surface%20technologies%20for%20components%20made%20from%20aluminium%20materials.pdf
[38] FRAUNHOFER IST. Electron beam hardening and hard coating for highly stressed tools and components [online]. [cit. 2015-05-21]. Available at: http://www.ist.fraunhofer.de/content/dam/ist/en/documents/weikai_elektron

enstrahlhaertung_en.pdf
[39] ASTM-C633, Standard Test Method for Adhesion or Cohesion Strength of Thermal Spray Coatings. 100 Barr Harbor Drive, West Conshohocken, PA 19429-2959: American Society for Testing and Materials, 1983.
[40] DICKINSON, Michelle E. a Motohiro YAMADA. A New Method for Measuring Shear Adhesion Strength of Ceramic Cold Spray Splats. *Nanoscience and Nanotechnology Letters*. 2010, **2**(4): 348-351. DOI: 10.1166/nnl.2010.1106.
[41] YUAN, Kang. *Thermal and Mechanical Behaviors of High Temperature Coatings*. 581 83, Linköping, Sweden, 2013. Thesis. Division of Engineering Materials, Department of Management and Engineering Linköping University.

# 7. List of Symbols and Shortcuts

| | | |
|---|---|---|
| A | [-] | Ratio of flattening velocity and impact velocity of the incident particle |
| D | [mm] | Splat diameter |
| D | [mm] | Initial particle diameter |
| DC | | Direct current |
| $E_1$; $E_2$; $E_3$; $E_4$ | [J] | Energy of the electron beam |
| EB | | Electron beam |
| $\Delta G$ | [J] | Gibbs free energy |
| $\Delta G_{surf}$ | [J] | Decrease of the Gibbs free energy due to surface energy |
| H | [mm] | TGO thickness |
| $\Delta H_c$ | [J] | Critical enthalpy of plasma gas |
| $\Delta H_s$ | [J] | Change of enthalpy because of different potential curves for atom combinations |
| HVOF | | High velocity oxygen fuel |
| I | [A] | Arc current |
| K | [-] | Flattening coefficient |
| $K_{cf}$ | [-] | Critical splashing flattening coefficient |
| $K_f$ | [-] | Splashing flattening coefficient |
| $k_p$ | [$g^2cm^4s^{-1}$] | Parabolic rate constant |
| mg | [kg-$s^{-1}$] | Mass flow rate |
| OFHC | | Oxygen-free high purity copper |
| $P_g$ | [W] | Dissipated power |
| $Q_e$ | [J] | Losses in the cooling unit |
| Re | [-] | Reynolds number |
| RF | | Radio frequency |
| $\Delta S_s$ | [$J.K^{-1}kg^{-1}$] | Increase in entrophy due to surface diffusion |
| T | [K] | Plasma temperature |
| T | [s] | time |
| TBC | | Thermal barrier coating |
| $T_{cont}$ | [K] | Contact temperature |
| TGO | | Thermally grown oxide |
| $T_t$ | [K] | Substrate temperature |
| VPS | | Vacuum plasma spray |
| $V_0$ | [$m^3$] | Liquid volume |
| We | [-] | Webber number |
| WSP | | Water stabilized plasma |
| YSZ | | Yttrium-stabilized zirconia |
| $\Sigma$ | [$N.m^{-1}$] | Liquid-gas surface tension |
| P | [$kg.m^{-3}$] | Liquid density |
| $\mu$ | [$N.s.m^{-2}$] | Liquid viscosity |

# 8. List of Figures

# 9. List of Tables